JGR Solid Earth

RESEARCH ARTICLE
10.1029/2020JB019847

Key Points:
- A compressional-wave speed model was built for the Greenland-Iceland Ridge crust
- The ridge may contain a substantial amount of preexisting continental crust
- The putative Iceland mantle plume can be considerably weaker than commonly thought

Correspondence to:
J. Korenaga,
jun.korenaga@yale.edu

Citation:
Yuan, X., Korenaga, J., Holbrook, W. S., & Kelemen, P. B. (2020). Crustal structure of the Greenland-Iceland Ridge from joint refraction and reflection seismic tomography. *Journal of Geophysical Research: Solid Earth*, *125*, e2020JB019847. https://doi.org/10.1029/2020JB019847

Received 24 MAR 2020
Accepted 26 MAY 2020
Accepted article online 29 MAY 2020

Crustal Structure of the Greenland-Iceland Ridge from Joint Refraction and Reflection Seismic Tomography

Xiaoyu Yuan[1], Jun Korenaga[2], W. Steven Holbrook[3], and Peter B. Kelemen[4]

[1]School of Geophysics and Information Technology, China University of Geosciences, Beijing, China, [2]Department of Earth and Planetary Sciences, Yale University, New Haven, CT, USA, [3]Department of Geosciences, Virginia Tech, Blacksburg, VA, USA, [4]Department of Earth and Environmental Sciences, Columbia University, Palisades, NY, USA

Abstract We report a reanalysis of active-source wide-angle seismic data collected along the Greenland-Iceland Ridge during the 1996 Seismic Investigation of the Greenland Margin (SIGMA) experiment. Interpreting the crustal structure of volcanic rifted margins has suffered from nonuniqueness because thick crust at the continent-ocean transition may not be totally of igneous origin. In this regard, the Greenland-Iceland Ridge presents a unique opportunity because, together with the Faroe-Iceland Ridge, it is generally considered to constitute the Iceland hotspot track, and as such, the bulk of its crust may be considered to be of igneous origin. From 15 ocean-bottom instruments deployed along a 290-km-long refraction transect, we collect 5,383 *Pg* and 1,118 *PmP* travel times, and we use joint refraction and reflection seismic tomography with adaptive importance sampling to invert them to construct a two-dimensional compressional wave speed (V_p) model across the Greenland-Iceland Ridge. Based on the covariation of crustal thickness and V_p, the western part of the transect may be almost entirely continental. Even the eastern part could include a significant fraction of preexisting continental crust. When considered together with the seismic structure of the Icelandic crust and its geochemical characteristics, our results suggest that the putative Iceland mantle plume could be considerably weaker than commonly assumed.

1. Introduction

The Iceland hotspot, widely considered to be the largest melt anomaly within the Earth's mid-ocean ridge system (Coffin & Eldholm, 1994), is one of the most thoroughly investigated hotspots, and its evolution is believed to play an important role in the tectonics of the North Atlantic (e.g., Skogseid et al., 2000). The hotspot is located on the oceanic spreading center of the North Atlantic and also lies on the aseismic Greenland-Iceland-Faroe Ridge (GIFR) between East Greenland and the Faroe Islands (Figure 1). The GIFR comprises two complementary regions: the Greenland-Iceland Ridge (GIR) crossing the Denmark Strait to the west and the Iceland-Faroe Ridge (IFR) to the southeast. This aseismic ridge, characterized by anomalously thick (>20 km thick) crust and shallow (<1 km deep) bathymetry (Bott, 1983; Brown & Lesher, 2014; Smallwood & White, 2002), constitutes the Iceland hotspot track (e.g., Lawver & Müller, 1994; Mihalffy et al., 2008; Torsvik et al., 2015) that formed during the opening of the North Atlantic. The seismic structure of the ridge thus is crucial to our understanding of the geodynamic processes that led to the development of the Iceland hotspot.

It is commonly thought that the Iceland hotspot is the surface expression of a deep mantle plume originating from the core-mantle boundary (Morgan, 1971), though there are a few variations for such a plume-based model. In the model of White and McKenzie (1989), for example, a plume is regarded as more or less a stationary feature, and the excess magmatism is generated by decompression melting of the hotter than normal mantle as a result of lithospheric stretching and rifting (see also Kelemen & Holbrook, 1995 for the U.S. East Coast margin). In the starting plume model (e.g., Griffiths & Campbell, 1990; Richards et al., 1989), on the other hand, a large plume head plays an active role in uplifting and breaking the lithosphere. Both of these plume models use the presence of the putative Iceland plume to explain the formation of the North Atlantic Igneous Province, that is, the occurrence of flood basalts along the North Atlantic margins that connected to the current Iceland hotspot through the paired GIR and IFR. In addition to these plume models, alternative mechanisms have also been suggested to explain the anomalous volcanism. In the secondary

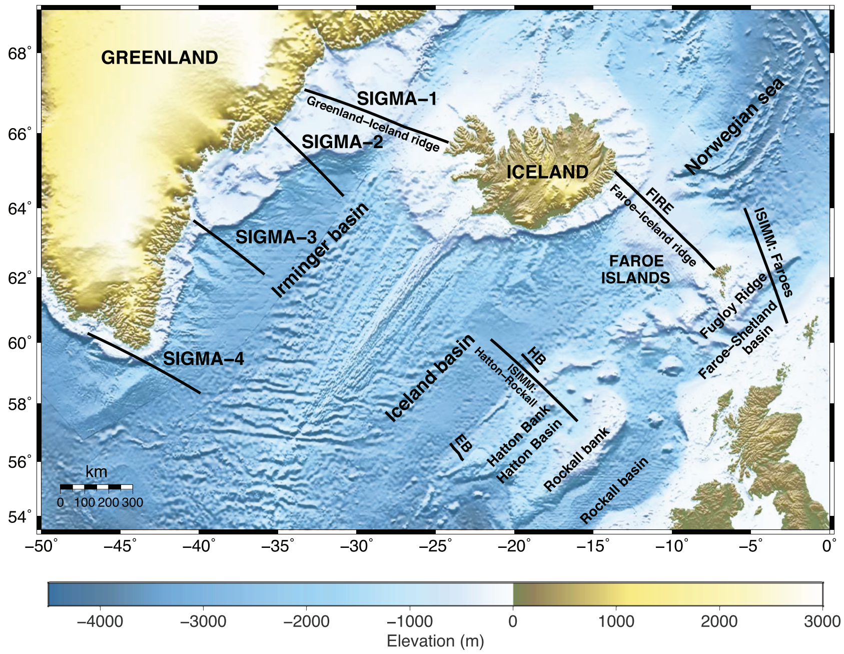

Figure 1. Location of major active-source seismic transects in the North Atlantic Igneous Province, including the SIGMA-1 transect, which is the focus of this study. SIGMA, Seismic Investigation of Greenland Margin (Holbrook et al., 2001). FIRE, Faroe-Iceland Ridge Experiment (Richardson et al., 1998). HB, Hatton Bank (Fowler et al., 1989; Morgan et al., 1989; White et al., 1987). EB, Edoras Bank (Barton & White, 1997). iSIMM, integrated Seismic Imaging and Modelling of Margins (Parkin & White, 2008; White & Smith, 2009; White et al., 2008).

upwelling model, for example, the melt anomaly results from asthenospheric convection enhanced by vertical thermal boundaries (e.g., Keen & Boutilier, 1995; Korenaga & Jordan, 2001, 2002; Mutter & Zehnder, 1988; Vogt, 1991; Zehnder et al., 1990). Moreover, major element heterogeneities in the source mantle can contribute to excess melting (Foulger & Anderson, 2005; Korenaga, 2004; Korenaga & Kelemen, 2000), and it has been suggested that Iceland might be a "wet" spot rather than a "hot" spot (Nichols et al., 2002; Vinnik et al., 2005).

To investigate the origin of the Iceland hotspot, a number of seismological studies have been conducted during the past few decades. Since seismic tomography can detect anomalies in seismic wave speed, depending on their diameter, hot mantle plumes may be imaged as columnar low-velocity anomalies caused by higher-than-normal temperatures. Some tomographic models show broad and relatively weak low-velocity anomalies below Iceland originating from the lower mantle (e.g., Bijwaard & Spakman, 1999; He et al., 2015; Helmberger et al., 1998; Montelli et al., 2006; Rickers et al., 2013; Yuan & Romanowicz, 2017), but it is not clear that they must represent a continuous plume conduit. Other tomographic studies agree on narrow but strong low-velocity anomalies in the upper mantle, but they differ in deeper mantle regions (e.g., Allen et al., 2002; Foulger et al., 2000; French & Romanowicz, 2015; Montelli et al., 2004; Ritsema et al., 2011; Wolfe et al., 1997). Receiver function methods can measure the depths of the major mantle discontinuities and provide additional constraints on the spatial extent of wave speed anomalies (e.g., Shen et al., 1998; Vinnik et al., 2005). Shen et al. (1998, 2002) imaged a locally thinned transition zone below Iceland, which was interpreted to represent a hot plume originating from the lower mantle. Such thinning of the transition zone is, however, not reproduced by a later similar study (Du et al., 2006), and a more recent receiver-function study suggests that the 660-km seismic discontinuity is depressed beneath Iceland, which could be attributed to garnet-dominated chemical heterogeneities (Jenkins et al., 2016).

Given the ongoing controversy of these mantle-based seismic studies, crustal seismology can provide unique constraints, and several attempts have been made to use the seismic structure of igneous crust to infer the dynamics of parental mantle (Kelemen & Holbrook, 1995; Korenaga et al., 2002; White & McKenzie, 1989). Quite a few active-source seismic studies have been conducted in the North Atlantic Igneous Province (e.g., Barton & White, 1997; Holbrook et al., 2001; Larsen & Jakobsdóttir, 1988; Mutter & Zehnder, 1988; Smallwood et al., 1999) (Figure 1), but only a few of them are published with comprehensive uncertainty analysis (e.g., Korenaga et al., 2000; Parkin & White, 2008; White & Smith, 2009), without which meaningful petrological interpretation is difficult. Korenaga et al. (2002), for example, found that a negative correlation between crustal V_p and thickness seen in the southeastern Greenland margin could not be explained by a purely thermal plume. They suggested that the formation of thick crust along the SIGMA-2 transect (Figure 1) required upwelling of chemically anomalous mantle (i.e., more fertile than the normal pyrolitic mantle). A similar negative correlation between crustal V_p and thickness was later found on the Hatton Bank transect as well, but White et al. (2008) interpreted the low V_p, thick part of their crustal transect to include preexisting continental crust with low V_p. They focused on explaining a positive correlation between V_p and crustal thickness in the thinner part of their transect, which may be interpreted as the effect of varying mantle temperature. Thus, whereas crust-based seismic studies provide important constraints independent from mantle-based studies, the interpretation of thick crust at volcanic rifted margins has its own difficulties, in part because the influence of preexisting continental crust is hard to rule out a priori in this tectonic setting. Given this controversy about the petrological interpretation of volcanic rifted margins, the crustal structure of the GIFR becomes particularly important; since it is the Iceland hotspot track, it may be safe to expect that the majority of this ridge is of igneous origin, avoiding the potential ambiguity associated with a gradual continent-ocean transition. At least, such a premise underlies the initial motivation for this study, which, as shown later, has yielded an unexpected outcome.

The main objective of this study is to estimate the crustal V_p structure of the Greenland-Iceland Ridge, using the SIGMA-1 transect acquired during the 1996 SIGMA experiment, a joint project between Woods Hole Oceanographic Institution (WHOI) and the Danish Lithosphere Centre. Both seismic reflection and wide-angle refraction data were collected along the four seismic transects from the southern tip of Greenland up to the Greenland-Iceland Ridge (Figure 1). A summary of all SIGMA transects was published by Holbrook et al. (2001). In-depth analyses of individual transects were reported for SIGMA-2 by Korenaga et al. (2000) and for SIGMA-3 by Hopper et al. (2003). Unfortunately, a full analysis of SIGMA-1 data has never been published, and the SIGMA-1 model in Holbrook et al. (2001) is not fully documented. Because the SIGMA-1 transect is along the presumed hotspot track, however, the extent of the rifting-to-spreading magmatism on this transect is critical to assess the effects of the putative Iceland plume. In this contribution, we use the joint refraction and reflection tomography of Korenaga et al. (2000), as amended by Korenaga and Sager (2012). Even though the SIGMA-1 transect was acquired more than 20 years ago, it provides sufficient data for such a tomographic inversion. The same cannot be said for active-source seismic data collected over the Iceland-Faroe Ridge (FIRE; Figure 1); because of the limited number of ocean-bottom instruments employed, the published FIRE crustal model suffers from large uncertainties (Richardson et al., 1998).

The structure of this paper is as follows. First, we describe the acquisition and processing of the SIGMA-1 seismic data. Then the two-dimensional (2-D) joint refraction and reflection tomographic inversion method (Korenaga & Sager, 2012; Korenaga et al., 2000) is used to invert wide-angle travel time data and estimate crustal velocity structure. The uncertainty and robustness of our velocity model are discussed in detail. We discuss possible petrological interpretations of the estimated seismic structure and close by speculating on their geological and geophysical implications.

2. Data Acquisition and Processing

The SIGMA-1 seismic data were acquired in 1996 using the R/V *Maurice Ewing*, with a 20-air gun, 8460 cubic inch tuned source array. A 290-km-long transect was shot between East Greenland and Iceland along the presumed track of the Iceland hotspot (Figure 1), with a shot interval of ~50 m (20 s). Wide-angle data were recorded on eight WHOI ocean-bottom hydrophones (OBH) and seven U.S. Geological Survey (USGS) ocean-bottom seismometers (OBS) deployed along the transect (Figure 2). There were also five REFTEK land stations deployed along the extension of the SIGMA-1 transect on Iceland, but these land recordings are not used in this study for two reasons. First, there is a ~150-km gap between the ocean-bottom array

10.1029/2020JB019847

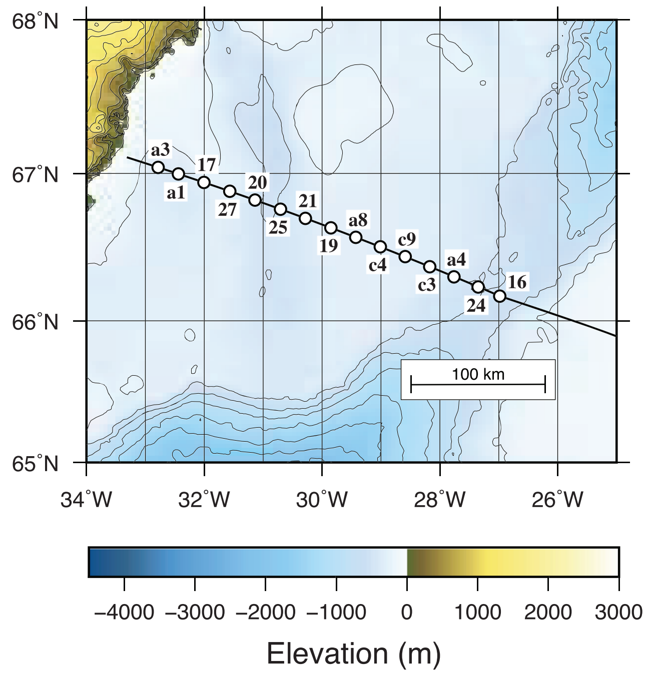

Figure 2. Configuration of SIGMA-1 transect seismic experiment. Circles denote ocean bottom instruments. Instrument names starting with alphabet (e.g., "a3") correspond to USGS ocean bottom seismometers and those with just numbers to WHOI ocean-bottom hydrophones. Contours are drawn at 500-m interval.

and the land stations, which poses a challenge for tomographic inversion. Second, there was no land seismic source, so it is impossible to use the source-receiver reciprocity to ascertain the consistency of phase identification, which is particularly important for late arrivals such as *PmP*, between ocean-bottom data and land data.

Owing to severe sea conditions, most of the wide-angle data along the SIGMA-1 transect are of moderate quality (Figure 3), although about half of the instruments show visible phases up to an offset of ~200 km (e.g., Figures 3b and 3g). The sampling interval was 10 ms, and we applied standard data processing including instrument relocation, bandpass filtering from 5 to 20 Hz, predictive deconvolution, and coherency weighting. The crustal refraction phase (including sedimentary arrivals), *Pg*, is observed in all record sections. The pattern of *Pg* is similar among different instruments; the apparent velocity of the *Pg* phase is ~4 to 6 km s^{-1} at near offsets and gradually reaches ~7.0 km s^{-1} at an offset of about 20 km (Figure 3). Strong lateral variations in the *Pg* arrival are seen in some record sections, which can be attributed to bathymetric features (e.g., Figures 3d and 3e) The reflection phase from the crust-mantle boundary (the Moho), *PmP*, can be seen in only some of the record sections, with variable quality.

In order to identify the seismic phases consistently across different record sections, the source-to-receiver reciprocity of travel times was exploited. Travel times were picked manually, and picking errors were assigned to be half a period of first cycle of an arrival, 50 ms for *Pg* and 100 ms for *PmP*, respectively. A total of 5,383 *Pg* and 1,118 *PmP* travel times were collected for the SIGMA-1 transect (Figure 4).

3. Joint Refraction and Reflection Tomography

The crustal seismic structure along the SIGMA-1 transect is estimated using the joint refraction and reflection tomography method of Korenaga et al. (2000) as amended by Korenaga and Sager (2012). We invert the travel times of both *Pg* and *PmP* phases simultaneously to build a 2-D compressional wave speed model with the geometry of the Moho. Our model domain is 290 km wide and 40 km deep from the seafloor, which is parameterized as a sheared mesh of nodes hanging from the seafloor with horizontal spacing of 1 km and vertical spacing increasing from 50 m at the seafloor to 1 km at the bottom of the model. The Moho is modeled as a floating reflector, which is represented as an array of linear segments of 291 nodes with a horizontal spacing of 1 km. Forward ray tracing for both refracted and reflected phases is done using the graph method with bending correction (Moser, 1991; Moser et al., 1992).

The fundamental components of tomographic inversion remain the same as in Korenaga et al. (2000), but the overall inversion framework follows the notion of adaptive importance sampling (Korenaga & Sager, 2012). In this framework, we apply smoothing constraints using vertically and horizontally varying correlation lengths, which are randomly sampled from their a priori ranges instead of determined by trial and error. We also use the automated regularization of Korenaga and Sager (2012) to determine appropriate smoothing weights, for which we set the maximum relative model variation to 0.5% for velocity nodes and 0.05% for depth nodes, respectively. As in Korenaga and Sager (2012), we use the normalized data misfit, χ^2/N, and a second model measure, R, to identify acceptable models. The data misfit χ^2 is here defined as the sum of squared difference between the observed and predicted travel times, in which each squared difference is divided by the variance of corresponding travel time data, and the normalized data misfit χ^2/N, where is N is the number of travel time data, is expected to be around unity for a model with reasonable data fit. The model measure R quantifies the overall model roughness, which is defined as an average relative deviation from the self-similar 1-D reference model. Larger values of R often correspond to geologically unrealistic velocity structures or models with too much small-scale variations (e.g., Figures 5c and 5d). Thus, models with $R>8$ are not considered in this study. By estimating how the data misfit and the model measure are

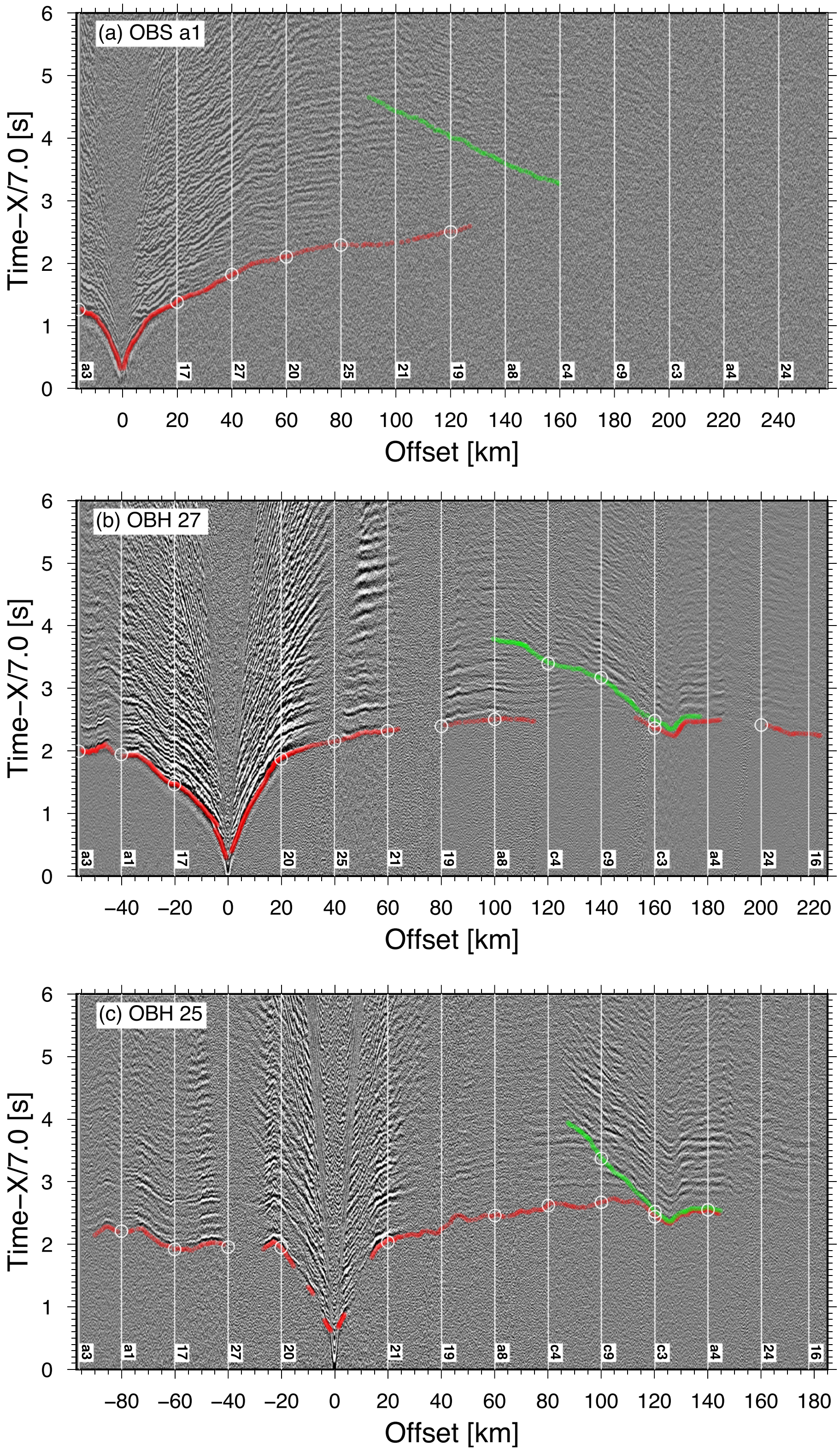

Figure 3. Processed seismogram for selected instruments, plotted with a reduction velocity of 7.0 km s^{-1}. Semitransparent markings denote the picked travel times of *Pg* (red) and *PmP* (green). White vertical lines denote the locations of other instruments, and circles correspond to their travel time picks at reciprocal relations (corrected for water-depth difference between instruments), demonstrating the consistency of phase identification among different instruments. (a) a1, (b) 27, (c) 25, (d) 19, (e) c4, (f) c3, and (g) 24.

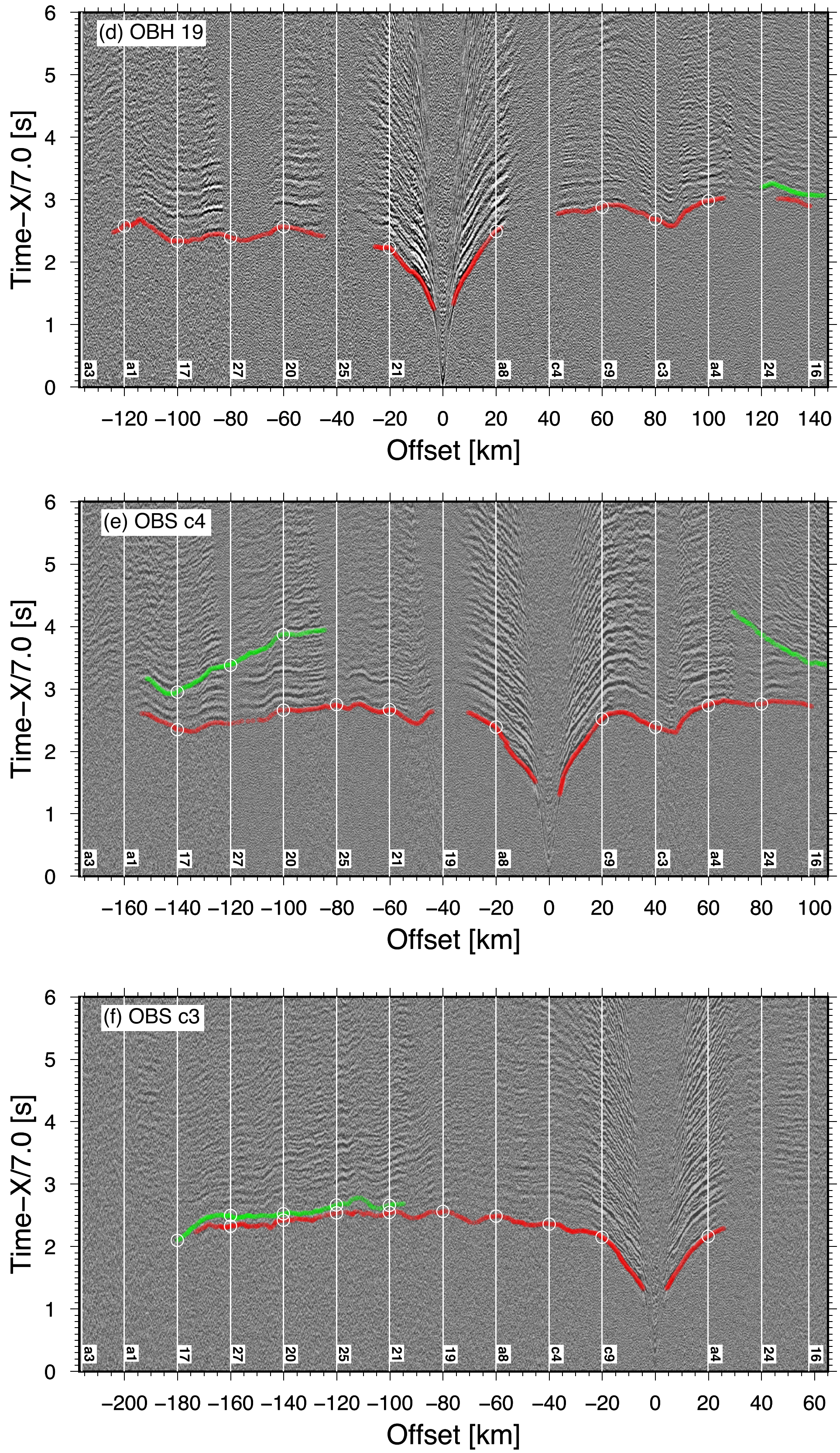

Figure 3. (continued)

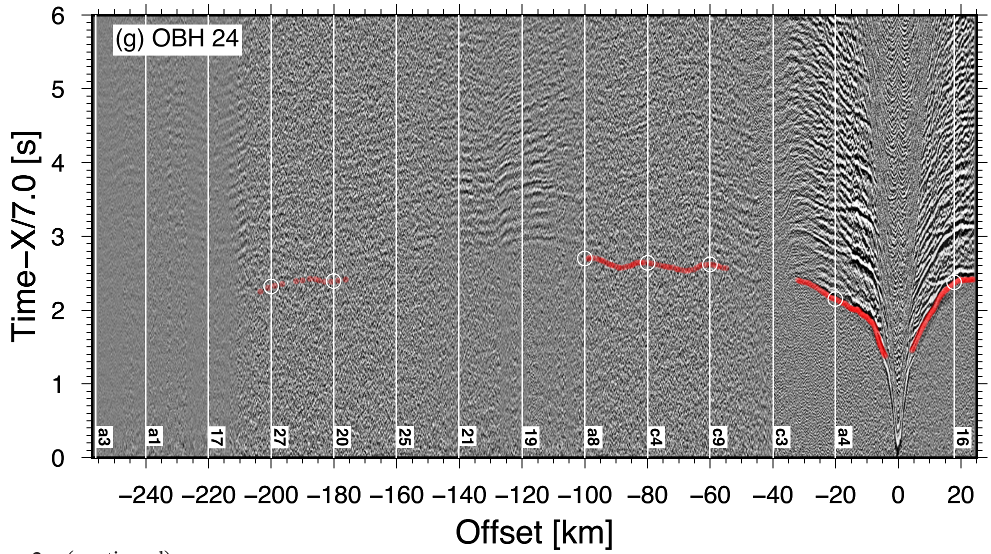

Figure 3. (continued)

related to the input model parameters, the efficiency of sampling becomes progressively improved, and a large number of successful models can be generated.

Our tomographic inversion starts with a 1-D initial average velocity model, which is constructed with the following equation:

$$V(z) = \begin{cases} V_{UC}^0 + (V_{MC}^0 - V_{UC}^0)\dfrac{z}{H_{UC}^0}, & z \le H_{UC}^0 \\ V_{UC}^0 + (V_{UC}^0 - V_{UC}^0)\dfrac{z - H_{UC}^0}{H_{LC}^0}, & z > H_{UC}^0 \end{cases} \tag{1}$$

where z is the depth measured from the base of the sedimentary layer, V_{UC}^0 is the upper-crustal velocity randomly chosen between 3 and 5 km s^{-1}, V_{MC}^0 is the midcrustal velocity between 5 and 7 km s^{-1}, V_{LC}^0 is the lower-crustal velocity between 7 and 8 km s^{-1}, H_{UC}^0 is the upper-crustal thickness between 3 and 9 km, and H_{LC}^0 is the lower-crustal thickness between 15 and 25 km. A flat initial reflector is used with its depth, Z_M^0, randomly sampled from 20 to 30 km. The sediment thickness along the SIGMA-1 transect is sampled from the global sediment thickness database of Straume et al. (2019).

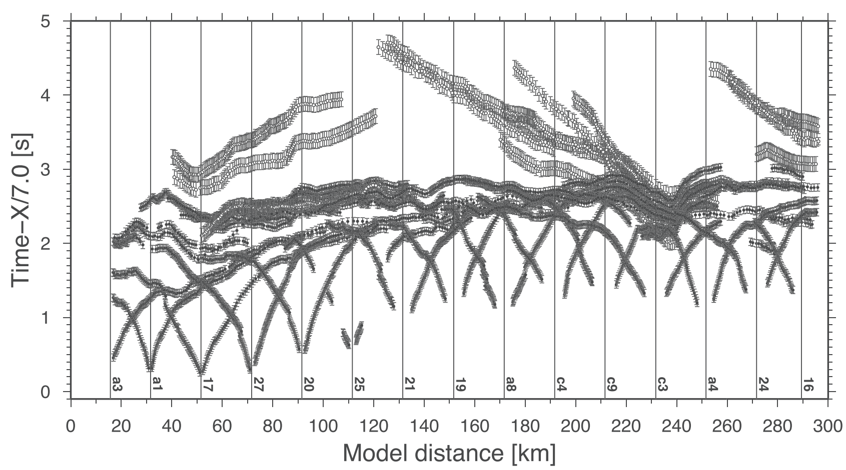

Figure 4. Picked travel times from all instruments are shown as a function of model distance, with their uncertainty. Vertical lines denote instrument locations. Solid and open circles are for *Pg* and *PmP*, respectively.

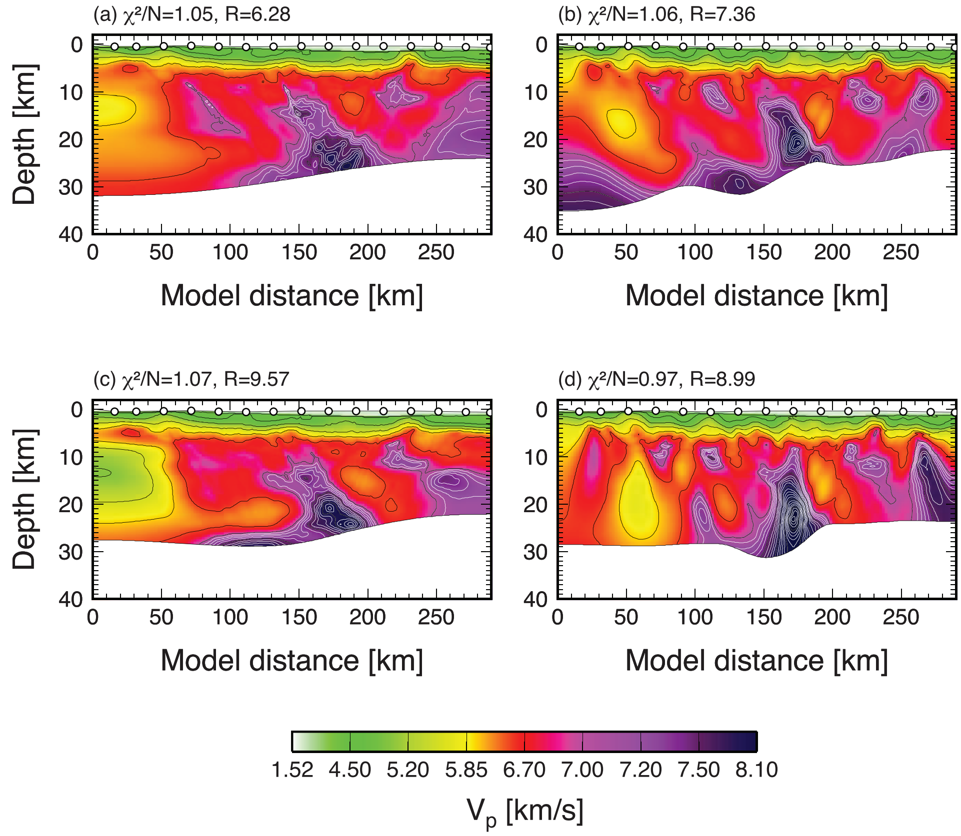

Figure 5. Examples of *P*-wave velocity models for SIGMA-1, obtained after 20 iterations, starting with different combinations of randomly chosen effective model parameters. Normalized χ^2 and the second model measure R are also shown for each model. They are all successful in terms of data fit, but some of them (those with R>8) indicate insufficient model regularization. Contours are drawn at an interval of 0.5 km s^{-1}, and additional contours are drawn in white at an interval of 0.1 km s^{-1} for V_p greater than 7.0 km s^{-1}.

The horizontal correlation length for smoothing is set as follows:

$$L_h(z) = \begin{cases} L_{h,UC} + (L_{h,MC} - L_{h,UC})\dfrac{z}{H_{UC}^L}, & z \le H_{UC}^L \\ L_{h,MC} + (L_{h,LC} - L_{h,MC})\dfrac{z - H_{UC}^L}{H_{LC}^L}, & z > H_{UC}^L \end{cases} \tag{2}$$

where $L_{h,UC}$, $L_{h,MC}$, and $L_{h,LC}$ are horizontal correlation lengths at $z = 0$, H_{UC}^L, $H_{UC}^L + H_{LC}^L$, respectively. These correlation lengths are sampled as follows. First, we sample $L_{h,UC}$ from a range between 2 and 30 km. We then set $L_{h,MC} = r_{Lh}L_{h,UC}$ and $L_{h,LC} = r_{Lh}L_{h,MC}$, where r_{Lh} is another random variable sampled from a range between 1 and 3. We also randomly sample H_{UC}^L between 3 and 9 km and H_{LC}^L between 15 and 25 km. The vertical correlation length is set similarly, with $L_{v,UC}$ and r_{Lv}, which are sampled between 1 and 3 km and between 1 and 3, respectively. The depth-kernel scaling parameter, w, is randomly sampled from a range between 10^{-2} and 10^2. The total number of effective model parameters (V_{UC}^0, V_{MC}^0, V_{LC}^0, H_{UC}^0, H_{LC}^0, Z_M^0, $L_{h,UC}$, H_{UC}^L, H_{LC}^L, r_{Lh}, $L_{v,UC}$, r_{Lv}, and w) is therefore 13 in this study.

At the beginning of the adaptive importance sampling scheme, we randomly sample M sets of model parameters from their a priori ranges (Figure 6, step 1). In the first inversion step, the data misfit χ^2/N of final models is modeled as a function of the effective model parameters (steps 2a and 3a). We then sample another M sets of effective model parameters, but this time, sampling is not entirely random; it is guided by the empirical functional relation between the model parameters and data misfit (step 4). In the subsequent

10.1029/2020JB019847

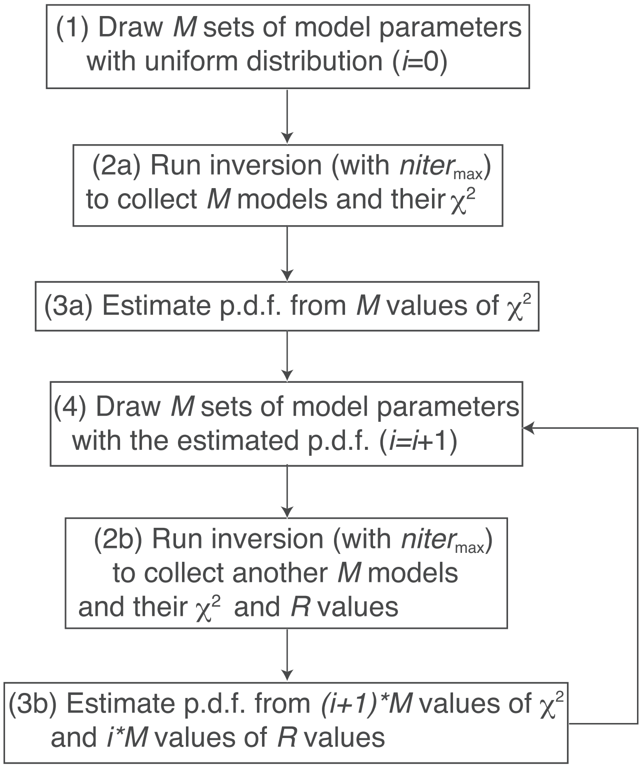

Figure 6. Flow chart for the adaptive importance sampling scheme of Korenaga and Sager (2012). The entire procedure is one long sampling "chain," which is composed of several "steps" (shown as boxes). Each inversion step (2a or 2b) contains M inversion "runs," and each inversion run conducts $niter_{max}$ iterations of tomographic inversion. For each inversion run, travel time data are also randomized with random common receiver errors and random travel time errors. "p.d.f." stands for probability distribution function.

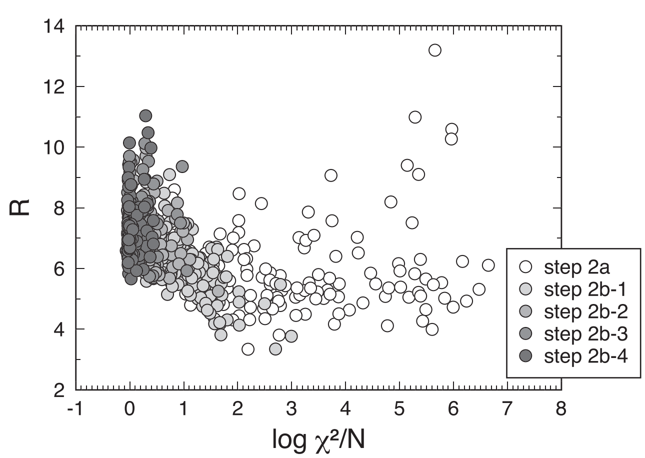

Figure 7. Covariation of normalized χ^2 and the second model measure R, through different stages of adaptive importance sampling. Trade-off between data fit and model roughness becomes clear at later stages.

steps, we also model the model measure R as a function of effective model parameters to make sampling more efficient (steps 2b and 3b). We reject parameter sets yielding χ^2/N>1 and R>8 and then periodically update the functional approximations for log(χ^2/N) and R by using all of previous inversion results (excluding inversion results of step 2a for R). For further details of the inversion scheme, see Korenaga and Sager (2012).

4. Results

We used $M = 200$,$niter_{max} = 20$, and $i_{max} = 4$ in the inversion strategy illustrated in Figure 6. A negative correlation is seen between the data misfit χ^2/N and the model roughness R as the inversion proceeds (Figure 7); that is, it is difficult to achieve both low χ^2/N and low R. In their tomographic analysis of Shatsky Rise data, Korenaga and Sager (2012) set the threshold for R as 5, but in this study, there is no model with χ^2/N~1 and R<5. This study is the second application of the adaptive importance sampling scheme of Korenaga and Sager (2012), and this difference in the the distribution of R values indicates that it may be necessary to vary the threshold value to accommodate different data sets.

Figure 8a shows how the distribution of χ^2/N gradually tightens in every step, indicating the efficiency of adaptive importance sampling. Because the initial sampling is done purely randomly from the given a priori ranges, the initial χ^2/N values are broadly distributed from ~0.5 to ~50, with most models having χ^2/N>1, whereas for the final velocity models, the corresponding χ^2/N values become clustered around unity (Figure 8a). Note that each inversion run conducts 20 iterations, and the value of χ^2/N after the final iteration can become smaller than unity. To avoid models that overfit data, therefore, we extract a model with χ^2/N closest to unity from each inversion run and call such a model the "optimal model."

Figures 8c–8o show the a posteriori probability distributions of effective model parameters. The results indicate that choosing appropriate values is important for some parameters for the inversion to be successful. Concerning an initial 1-D velocity model, for example, the inversions were more successful if the initial upper-crust velocity V^0_{UC} and the initialmidcrust velocity V^0_{MC} were in the ranges of 4.5–5 km s^{-1} (Figure 8c) and 6–6.7 km s (Figure 8d), respectively, and if the initial depth of the Moho was shallower than 27 km (Figure 8h), whereas the successful range of values for other parameters (V^0_{LC}, H^0_{UC}, and H^0_{LC}) were more uniform. Also, inversions were more successful when the horizontal correlation length $L^{h,UC}$ was smaller than 5 km (Figure 8i) with r^{Lh}<1.4 (Figure 8k) and when the vertical correlation length $L^{v,UC}$ was less than 1.5 km (Figures 8j) with r^{Lv}<1.6 (Figure 8l).

4.1. Mean and Variance

The mean and standard deviation for the initial models of all successful inversion runs are shown in Figures 9a and 9b, respectively. For the corresponding optimal models, that is, the models with χ^2/N~1, the mean and standard deviation are shown in Figures 9c and 9d, respectively. At less than 20–30 km from the edges of the model domain, the model suffers from large uncertainties (Figure 9d), and these parts are not used in the discussion (section 5). The standard deviation of velocity nodes is generally less than 0.2–0.3 km s^{-1}, except for the lower-crustal regions

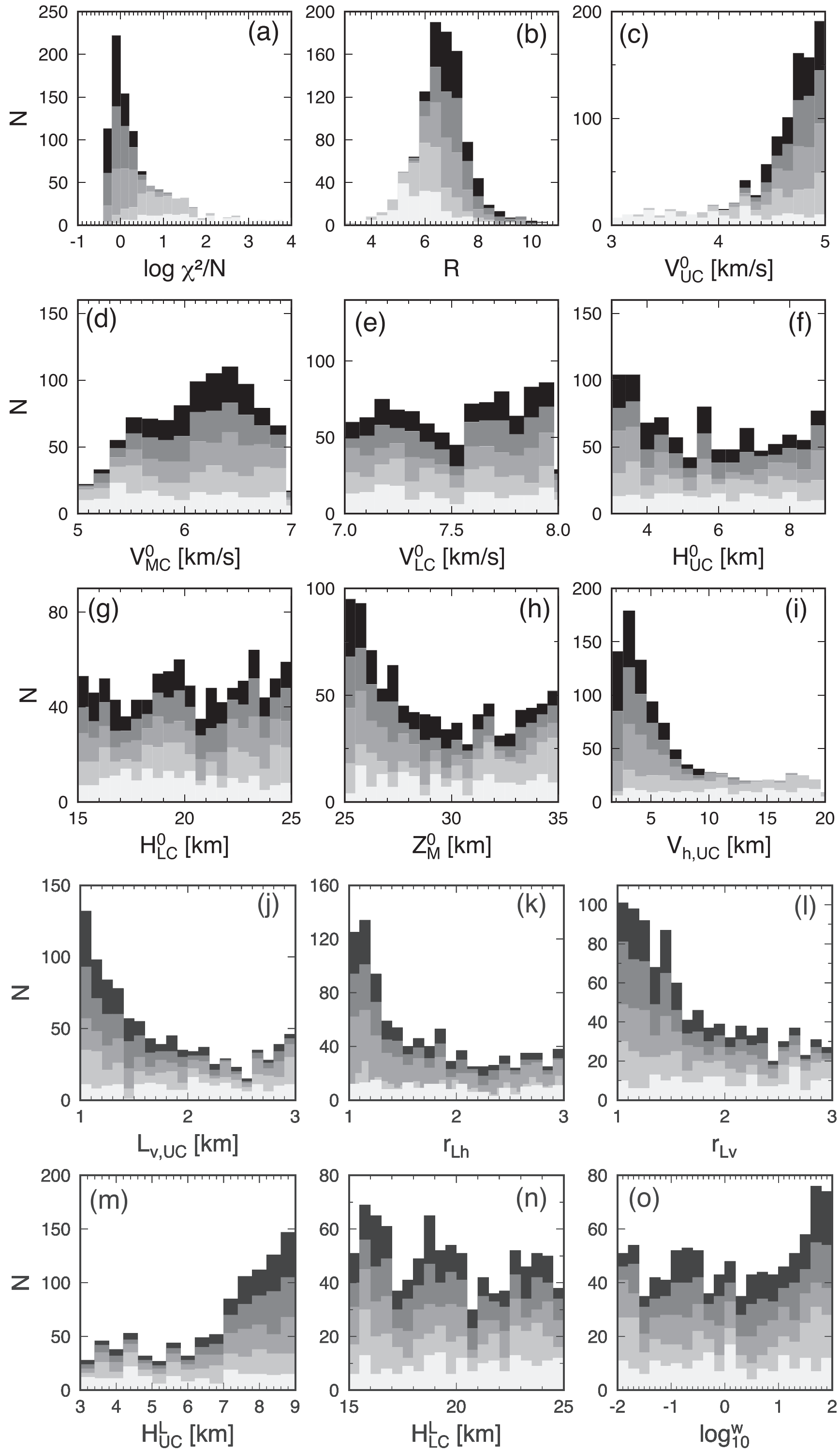

Figure 8. A posteriori distributions of model diagnostics and effective model parameters. The shade of each histogram changes gradually from the lightest ($i = 0$) to darkest ($i = 4$) to clarify progression through a sampling chain. (a) Normalized χ^2, (b) model measure R, (c) initial upper-crustal velocity, (d) initial midcrustal velocity, (e) initial lower-crustal velocity, (f) initial upper-crustal thickness, (g) initial lower-crustal thickness, (h) initial Moho depth, (i) horizontal correlation length for upper crust, (j) vertical correlation length for upper crust, (k) scaling constant for horizontal correlation length, (l) scaling constant for vertical correlation length, (m) upper-crustal thickness for correlation-length function, (n) lower-crustal thickness for correlation-length function, and (o) depth-kernel scaling parameter.

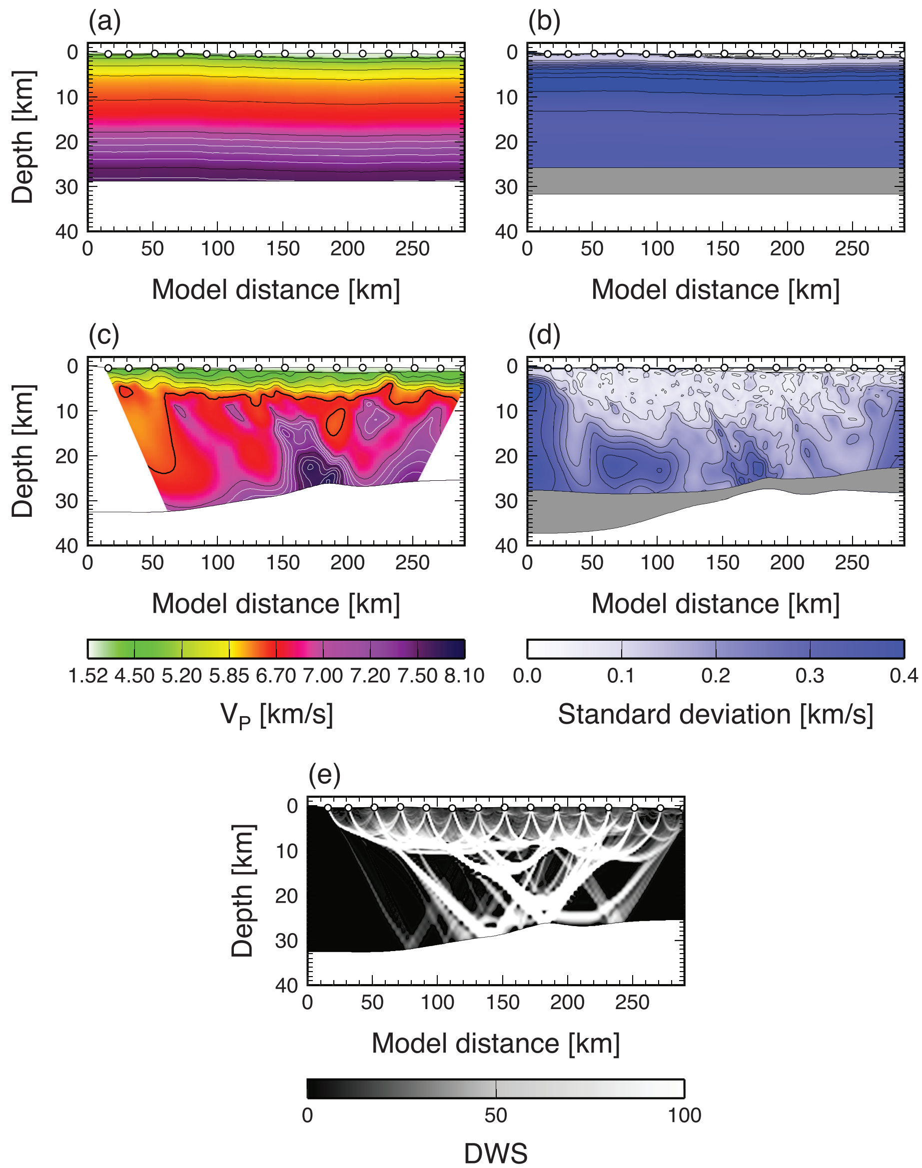

Figure 9. Summary of inversion results for the SIGMA-1 transect. (a) The average of initial models corresponding to ~400 successful runs (i.e., with the final $\chi^2/N<1$ and $R<8$). (b) The standard deviation of those initial models. Gray region denotes the range of one standard deviation for initial reflector depths. (c) The average of optimal models ($\chi^2/N\sim1$) chosen from the successful runs. The contour of 6.5 km s^{-1}, which is used to divide upper and lower crust, is shown in bold. The edges of the model that are unlikely to have been sampled during iterative inversion are masked. (d) The standard deviation of those models. (e) Derivative weight sum, which may be regarded as a proxy for ray density, for the average model shown in (c). Open circles along sea floor denote the location of ocean-bottom instruments. Contours are drawn at an interval of 0.5 km s^{-1} for (a) and (c) and 0.05 km s^{-1} for (b) and (d). For (a) and (c), additional contours are drawn in white at an interval of 0.1 km s^{-1} for V_p greater than 7.0 km s^{-1}.

between km 60–110 and km 160–190. The standard deviation for depth nodes is from ~1 km in the middle to ~5 km on the left edge and to ~2 km on the right edge. The crustal thickness varies almost linearly from ~32 km in the northwestern end to ~26 km in the southeastern end. Throughout the model domain, vertical V_p gradients show a marked change at about 6.5 km s^{-1}, and we divide the crust into the high-V_p-gradient upper-crustal section and the low-V_p-gradient lower-crustal section at the 6.5 km s^{-1} contour.

The derivative weighted sum (DWS) (Toomey & Foulger, 1989) shown in Figure 9e provides a quantitative measure of the density of seismic rays based on the average model of Figure 9c. The lower crust is sparsely

10.1029/2020JB019847

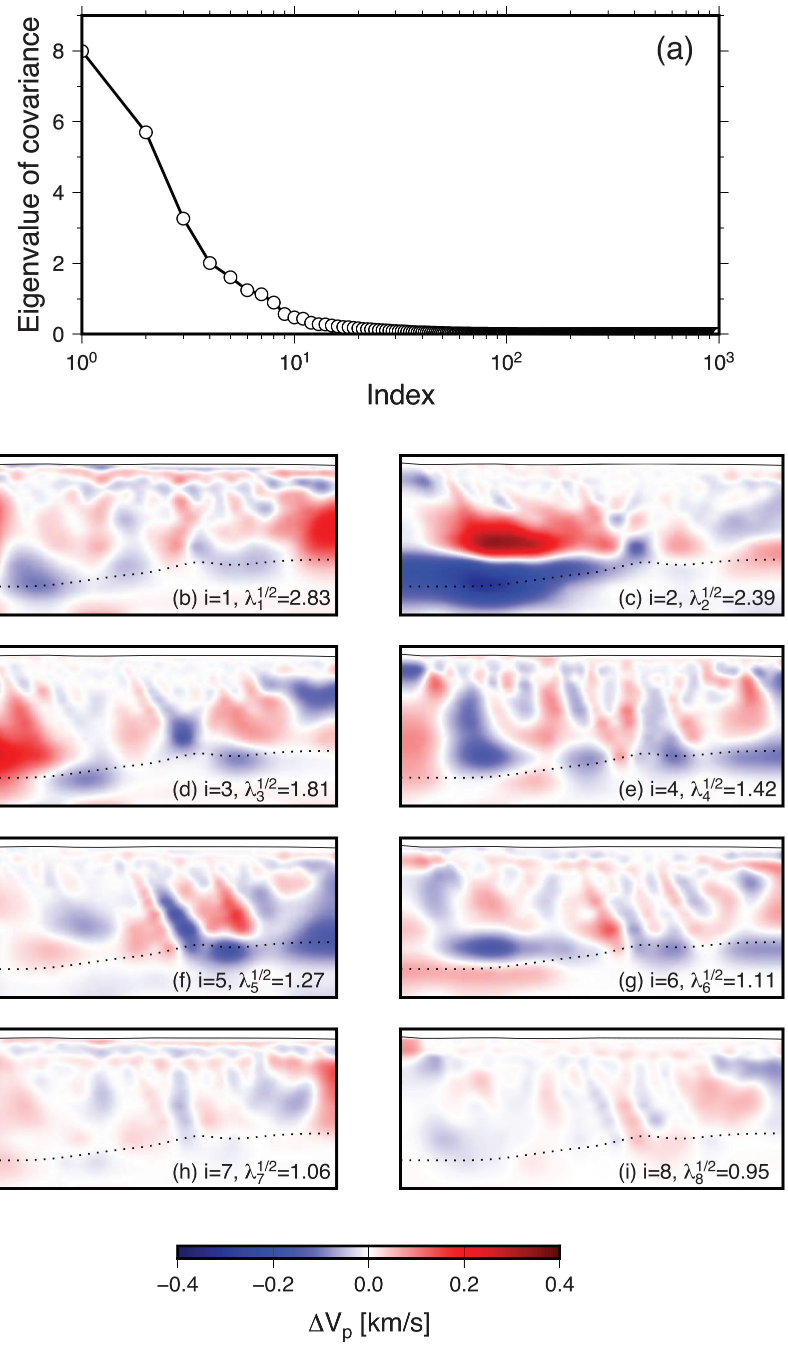

Figure 10. Results of principal component analysis of the ensemble of optimal models. (a) Eigenvalues of the covariance matrix shown in order of decreasing magnitude and (b–i) scaled eigenmodes corresponding to the first to eighth eigenvalues. Dotted curve denotes the average Moho as shown in Figure 9c.

covered by reflection and refraction, implying moderate resolution for that part of the model. Because the calculation of DWS is based on just one velocity model, it does not contain information regarding all other models that are tested during iterative inversion. On the other hand, the model uncertainty shown in Figure 9d is based on a large number of models collected during Monte Carlo sampling. Thus, by comparing DWS and the model uncertainty, we can discuss the nonlinear sensitivity of iterative inversion (e.g., Korenaga, 2011; Zhang, 1997). For example, the lower crust between km 100–150 and km 200–250 is only sparsely sampled by reflection rays in the average model but has relatively small standard deviations,

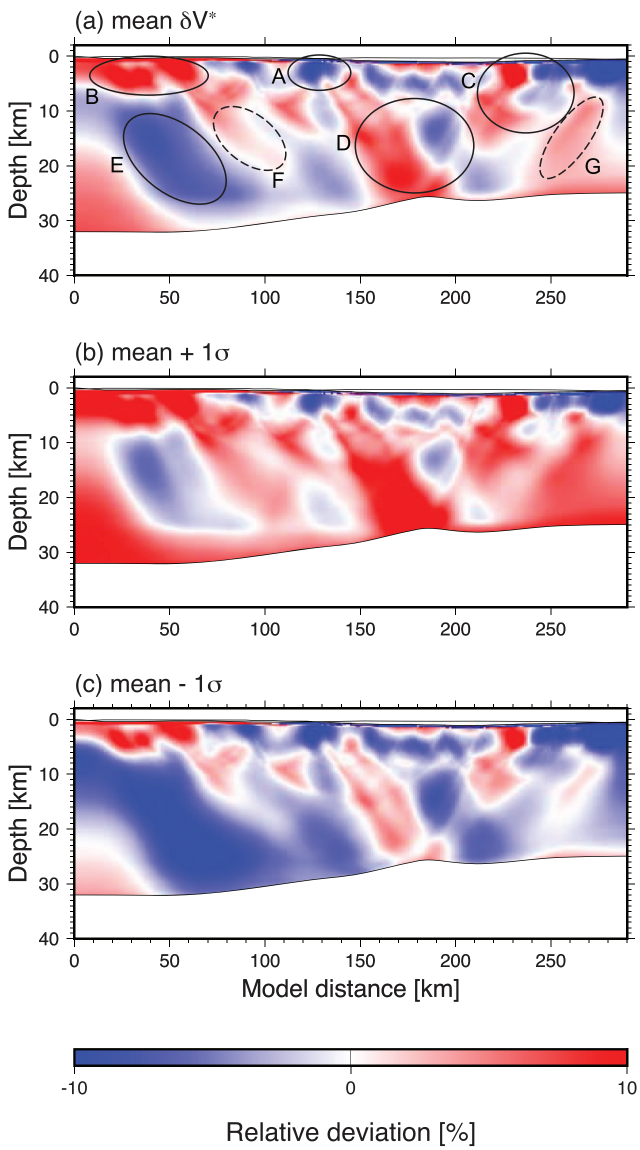

Figure 11. Statistics of relative model deviation δV^* (Equation 3): (a) mean, (b) mean plus one standard deviation, and (c) mean minus one standard deviation.

and the converse is true for the the lowermost crust between km 160–190. What this means is that the sparsely sampled parts of the final velocity model have been more intensively sampled during previous iterations. We can also recognize the influence of regularization as well as the a priori range of the effective parameters on model uncertainties (Figure 9d); the standard deviation near the edges, which are not sampled by any rays, is large but still finite (0.3–0.4 km s^{-1}) because of the smoothing constraints.

Compared to the original SIGMA-1 velocity model seen in Holbrook et al. (2001), our new velocity model (Figure 9c) is generally characterized by lower V_p and slightly thinner crust. Whereas regions with V_p greater than 7.0 km s^{-1} are limited in the new model (most notably in the lower half of the crust between km 150–200), the bottom 2/3 of the lower crust in the old SIGMA-1 model exhibits V_p greater than 7.0 km s^{-1} almost uniformly along the entire transect (see Figure 2 of Holbrook et al., 2001). The more localized high V_p feature in the new model is probably owing to the flexible model parameterization of the tomography of Korenaga et al. (2000). In addition, thanks to depth-kernel scaling, our tomography can extensively explore velocity-depth trade-off associated with *PmP*, which can be significant when the crust is thick. With a reference crustal thickness of 30 km, for example, a 1 km difference in thickness corresponds to ~0.2 km s^{-1} difference in V_p, for the same vertical-incidence travel time. Given the relatively large model uncertainties (Figure 9d), the old SIGMA-1 velocity model is within two standard deviations of our mean model; the old model can be seen as an end member with higher crustal V_p and thicker crust. This is similar to what is seen in the reanalysis of seismic data collected over the Ontong Java Plateau (Korenaga, 2011) (see their Figure 8a).

4.2. Eigenmodes

Besides standard deviation, we also calculate the full covariance matrix using the ensemble of optimal models. Using the original model parameterization would result in a large dense matrix, which requires excessive memory consumption, so we decimated the velocity mesh down to 73×20. This approach is justified by the smooth nature of tomographic models. Prior to the decimation, the information of the depth nodes was incorporated into the velocity mesh, by replacing the V_p nodes below the Moho reflector with a mantle V_p of 8.2 km s^{-1}. To extract the essence of the model covariance matrix, we conduct the principal component analysis as outlined in Korenaga and Sager (2012). The eigenvalues of the covariance matrix are shown in order of decreasing magnitude in Figure 10a. It can be seen that $\lambda_i/\lambda_1 \ll 1$ for $i > \sim 10$, and this means that the effective dimension of the model space, consistent with the given data and regularization, is no more than 10. Linear combinations of just 10 eigenvectors are sufficient to approximate a large number of models collected through Monte Carlo sampling. Figures 10b–10i display the scaled eigenmodes, defined as eigenvectors multiplied by $\lambda_i^{1/2}$, which illustrate the most significant parameter correlation and trade-off. The scaled eigenmodes have the dimension of wave speed, and they are listed in order of their amplitudes. The first scaled eigenmode represents the uncertainty associated with the edges of the model (Figure 10b), and the second eigenmode corresponds to the uncertainty in the lower-crustal V_p, especially in the western part of the transect (Figure 10c). The third to sixth eigenmodes all exhibit relatively large V_p trade-offs in the lower crustal section (Figures 10d–10g), which most likely originate in the paucity of *PmP* travel times. In any event, the number of optimal models collected in this study (~400) is far greater than the effective dimensions of the model space, suggesting that our Monte Carlo sampling is reasonably exhaustive.

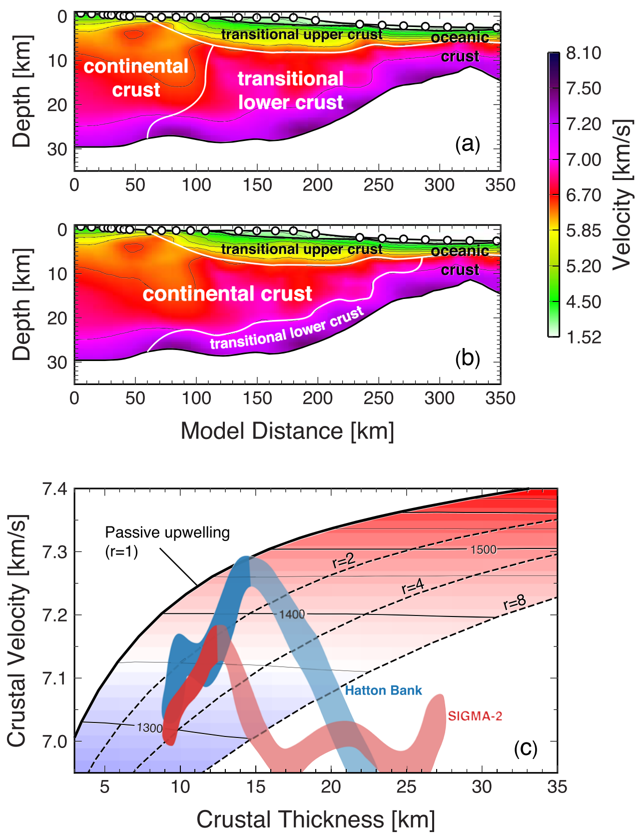

Figure 12. (a) The average *P*-wave velocity model for the SIGMA-2 transect (Korenaga et al., 2000), with the geological interpretation of Korenaga et al. (2002). (b) Same as (a) but with an alternative interpretation in a style similar to that of White et al. (2008). (c) Covariation of whole crustal thickness and the average *P*-wave velocity of lower crust for SIGMA-2 (red) and Hatton Bank (blue) transects. Dimmed shading indicates covariation with negative correlation between velocity and thickness, which may reflect either anomalously fertile source mantle or extended continental crust. Also shown in the background is a possible petrological interpretation based on the method of Korenaga et al. (2002). Nearly horizontal contours denote mantle potential temperature in °C, which is also shown in color shading (white corresponding to the present-day ambient mantle temperature, 1350°C; Herzberg et al., 2007). Other more diagonal contours correspond to different ratios of active mantle upwelling (r), and thick curve represents the standard case of passive upwelling beneath a mid-ocean ridge ($r = 1$). Theoretical crustal velocities are values expected at a pressure of 600 MPa and temperature of 400°C.

4.3. Spatial Resolution

Different attempts have been made to assess the spatial resolution of a tomographic model, for example, by conducting checkerboard tests (e.g., Lévěque et al., 1993; Rawlinson et al., 2014) or by calculating correlation coefficients (Zhang & Toksöz, 1998). However, checkerboard tests can only evaluate linear sensitivity, and correlation coefficients are not simply related to spatial resolution. Another popular approach is to calculate a resolution matrix via the singular value decomposition of a sensitivity kernel (Aster et al., 2005), but the notion of resolution matrix is also based on linear inverse theory, thereby being unable to take into account nonlinear sensitivity.

Korenaga and Sager (2012) suggested that, for nonlinear travel time tomography, spatial resolution may be assessed by calculating the statistics of the relative model deviation defined as

$$\delta V^*(x, z) = \frac{V(x, z)}{V_{\text{ref}}(z/h(x))} - 1\,, \tag{3}$$

in which $h(x)$ is crustal thickness, and $V_{\text{ref}}(\cdot)$ is a horizontally averaged velocity profile calculated as

$$V_{\text{ref}}(z') = \int V(x, h(x)z')dx \Big/ \int dx. \tag{4}$$

Here the normalized coordinate z' ranges from 0 to 1. Thus, we can extract information on spatial resolution directly from the ensemble of optimal models, in a very simple manner. Our primary concern when evaluating spatial resolution is the reliability of small-scale features, and it is straightforward to assess such reliability using the statistics of the relative deviation (Figure 11). Regions with positive deviations occur where velocity values are persistently higher than a 1-D reference model, and the converse is true for regions with negative deviations. The upper crust beneath around km 130 is, for example, characterized by a highly localized negative deviation (region A in Figure 11a), and it is a robust feature because the negative deviation persists even when standard deviations are taken into account (Figures 11b and 11c). A pair of positive and negative patches in the upper crust around km 240 (region C) is also persistently seen in all of these figures, so it is a robust feature as well. On the other hand, weak positive deviation observed in the lower crust around from km 70 to km 110 (region F) and from km 250 to km 270 (region G) are not robust because their positiveness diminishes in Figure 11c. Surprisingly, a positive and negative pair in the lower crust (region D) is also a persistent feature, even though major eigenmodes (Figure 10) suggest that the lower crust suffers considerably from several velocity trade-offs. In other words, understanding trade-offs among model parameters alone may not be sufficient to determine the robustness of certain model features. The negative deviation near the western end (region E) is also a surprisingly robust feature given a low ray density coverage (Figure 9e). Indeed, the standard deviation of the average velocity model is relatively low for this region despite large uncertainty in the corresponding Moho depth (Figure 9d). The interpretation of these robust features will be discussed in section 5.2.

5. Discussion

5.1. How to Treat the Continent-Ocean Transition

Before interpreting the SIGMA-1 crustal velocity model, we first review the existing debate on how to interpret the velocity structure of thick crust typically observed at the continent-ocean transition of volcanic rifted

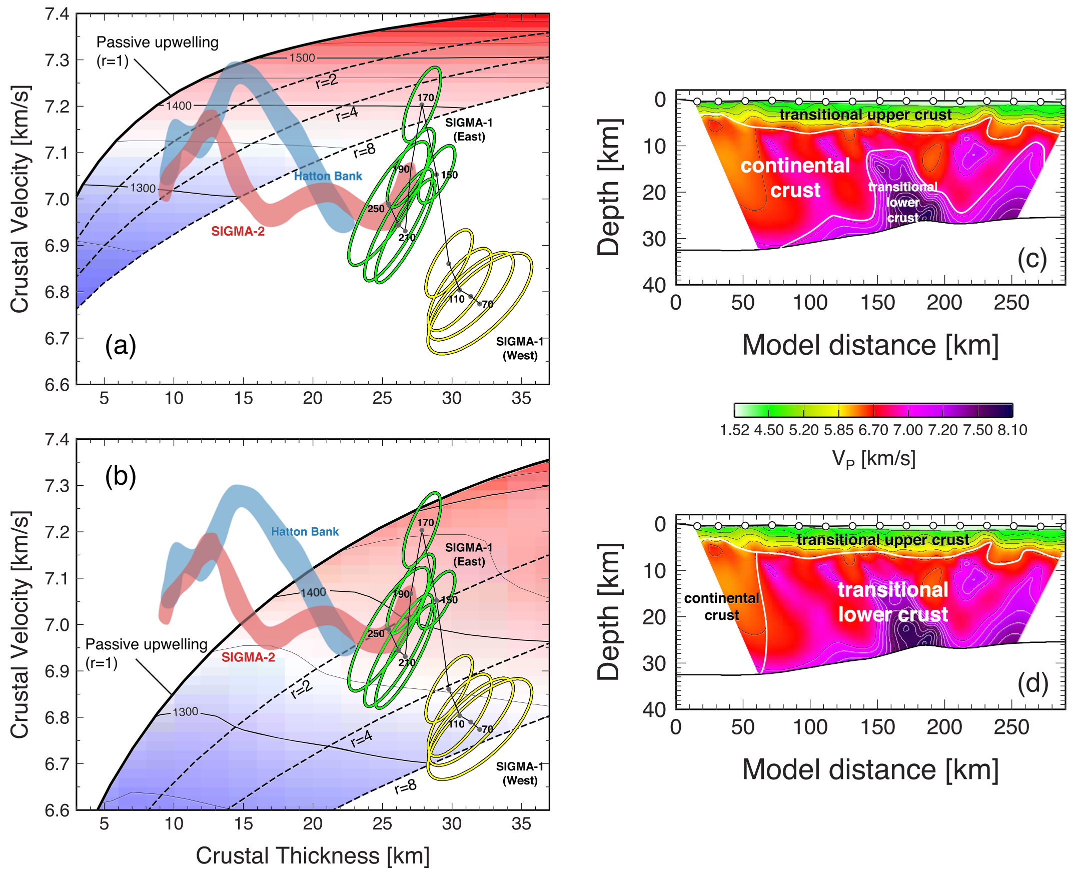

Figure 13. (a) Same as Figure 12c but with data from the SIGMA-1 transect. Average lower-crustal velocity and whole-crustal thickness are calculated from km 70 to km 250 at an interval of 20 km with a 20-km-wide averaging window, using all of 401 optimal models. See text for further details. Ellipses denote the 68% confidence region of whole crustal thickness and lower-crustal velocity, and gray dots denote their mean values. Yellow and green ellipses represent the western and eastern sections of the transect, respectively, and model distance (in km) is shown next to gray dots. (b) Same as (a) but with the background corresponding to a hypothetical high-Fe source mantle composed of 70% depleted pyrolite mantle and 30% MORB (Korenaga et al., 2002). (c) The average *P*-wave velocity model for the SIGMA-1 transect (Figure 9c) with the geological interpretation similar to Figure 12b. (d) Same as (c) but in a style similar to Figure 12a.

margins, because this interpretational issue has a long and convoluted history. This issue has three parts: (1) the meaning of high-velocity lower crust, (2) the accuracy of crustal velocity models, and (3) the influence of preexisting continental crust. Whereas these three parts are technically independent of each other, they have been contextually intertwined, as described below.

The discovery of large high-velocity (i.e., *P*-wave velocity higher than 7.3 km s^{-1}) lower crust at the Hatton Bank in the North Atlantic (White et al., 1987), combined with theoretical understanding of mantle melting (McKenzie & Bickle, 1988), led to a general interpretational framework for the crustal structure of volcanic rifted margins (White & McKenzie, 1989). Put simply, a hotter mantle melts more extensively, creating thicker crust, and because a higher degree of melting increases the olivine content of resulting igneous crust, thicker crust is characterized with higher crustal V_p as well. Thus, thick, high-V_p crust found at the Hatton Bank can be interpreted as a result of the upwelling of an unusually hot mantle, and such an interpretation conforms to various mantle plume hypotheses. This simple framework has long been influential, with a few variants in the literature (e.g., Kelemen & Holbrook, 1995; Korenaga et al., 2002; Richards et al., 2013; Sallares et al., 2005).

This interpretation of high-velocity lower crust is, however, problematic at least for two reasons. First, the volume of such high-velocity crustal body may not be as large as suggested by the classic study of White et al. (1987); this is an issue of geophysical inference, which will be discussed in some detail later. Second, high-velocity lower crust does not necessarily require the melting of a hotter-than-normal mantle. Zehnder et al. (1990) first noted that gabbroic rocks sampled from normal oceanic crust (including ophiolites) typically have a P-wave velocity of ~7.3 km s^{-1} (e.g., Christensen & Smewing, 1981), and they interpreted the high-velocity lower crust found at the Vøring margin as the result of active upwelling of normal mantle, although they did not explain why the P-wave speed of normal oceanic lower crust was only ~6.9 km s^{-1} (White et al., 1992). On the basis of petrological modeling (Korenaga et al., 2002) and calculated mineral proportions combined with elastic constants for minerals (Behn & Kelemen, 2003), one possible explanation is that the P-wave speed of normal oceanic lower crust should be as high as ~7.3 km s^{-1}, because of the cumulate nature of the lower crust, but is lowered to ~6.9 km s^{-1}, by the effects of crack porosity and seawater alteration. Because both porosity and alteration are expected to be reduced at greater depths, high-velocity lower crust is expected when crustal thickness is greater than normal, even with the same crustal composition. Crack-related porosities are expected to result from thermal contraction of igneous crust (Korenaga, 2007); theoretical considerations suggest the formation of cascade crack system with narrowly spaced shallow cracks and widely spaced deep cracks, and the depth of cracks are on the same order of their spacing. For example, 5-km-deep thermal cracks are expected to form at a ~5-km interval. The maximum depth of thermal cracks grows with the cooling of oceanic lithosphere, and it can reach >20 km depth at 50-Ma-old lithosphere (Korenaga, 2007). The pervasive existence of thermal cracks in the oceanic lithosphere has some observational support as well (Chesley et al., 2019; Korenaga, 2017; Korenaga & Korenaga, 2016); we also note that the V_p/V_s ratio observed for the oceanic crust part of the Hatton Bank transect (Eccles et al., 2011) is consistent with the prediction of crack-like porosity (Korenaga, 2017). Thus, a positive correlation between crustal velocity and thickness may simply result from the closure of porosities at greater pressures (see, e.g., Figure 14 of Behn & Kelemen, 2003 and related references), especially when oceanic crustal thickness is not very different from the standard value of 7 km (White et al., 1992); note that, with thermal gradient fixed, thicker crust leads to higher average temperature, which acts to reduce crustal velocity, but this effect is small (only ~0.025 km s^{-1} difference between crustal thicknesses of 5 and 10 km) because of a counteracting pressure effect on seismic wave speed (White & McKenzie, 1989). As the upper crust is always subject to the effect of porosity and alteration, the lower crust of thicker-than-normal oceanic crust is the only useful part for petrological interpretation, and given its likely cumulate nature (which results from fractional crystallization), its P-wave speed should be taken as an upper bound on the bulk crustal velocity (Korenaga et al., 2002).

The above development in the petrological interpretation of igneous crust was concurrent with the progress of seismic data acquisition and analysis. Inferring a 2-D crustal structure by interpolating a series of 1-D velocity models obtained from expanding spread profiling was popular during the 1980s (e.g., Mutter & Zehnder, 1988; White et al., 1987), but estimating a 2-D structure directly by modeling the travel time data of ocean-bottom seismometers became more common in the following decade (e.g., Barton & White, 1997; Holbrook et al., 1994; Mjelde et al., 1998). Eventually, tomographic imaging with both refraction and reflection travel time data has become possible (e.g., Zhang et al., 1998). The analysis of the SIGMA-2 data provided the first example of a tomography-based model for a volcanic rifted margin, with its uncertainty quantified by nonlinear Monte Carlo analysis (Korenaga et al., 2000). The SIGMA-2 crustal structure, however, turned out to be a challenge for petrological interpretation. Holbrook et al. (2001) and Korenaga et al. (2002) interpreted the SIGMA-2 velocity model as shown in Figure 12a. Figure 12c shows how the average lower-crustal V_p (excluding the continental crust) varies with total crustal thickness. The thick (>15 km) part of transitional crust is characterized by an average V_p of ~7.0 km^{-1}, which is difficult to interpret in terms of mantle dynamics; if taken at face value, the formation of such crust requires very vigorous active upwelling (with an active upwelling ratio of ~16) of a colder-than-normal mantle (the potential temperature of ~1300°C). As an alternative interpretation, Korenaga et al. (2002) suggested that the source mantle of the North Atlantic igneous province was more fertile than the normal pyrolitic mantle. Melting of an anomalously fertile mantle with moderate active upwelling can produce thick crust with low V_p. The existence of such source mantle heterogeneities is consistent with the geochemistry of lavas in the North Atlantic Igneous Province (Korenaga & Kelemen, 2000; Shorttle & Maclennan, 2011).

The 1996 SIGMA experiment was followed by another major data acquisition effort in 2002 (called iSIMM) on the conjugate European margin. Its main results were published by White et al. (2008). They revisited the

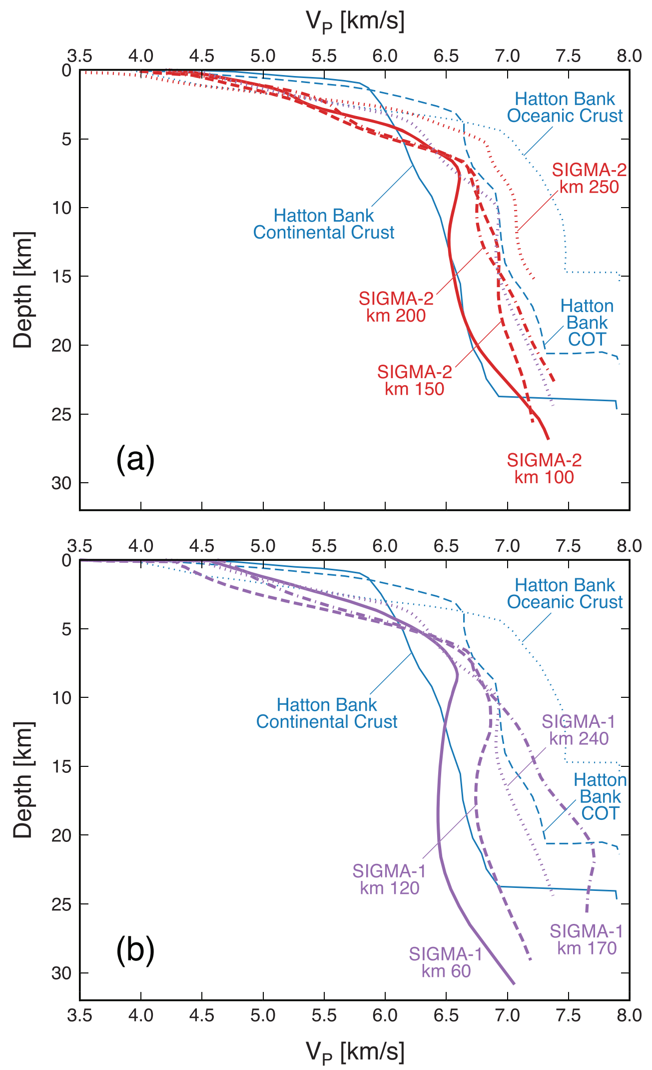

Figure 14. Representative vertical velocity profiles from (a) the SIGMA-2 transect (red) and (b) the SIGMA-1 transect (purple). Three profiles from the Hatton Bank transect (White et al., 2008) are also shown for comparison: continental crust (blue solid), continent-ocean transition (blue dashed), and oceanic crust (blue dotted). Each transect from SIGMA-1 and SIGMA-2 transects is based on the average model (Figure 9c), with horizontal averaging of ±10 km.

Hatton Bank transect, this time with a dense array of ocean-bottom seismometers, and conducted tomographic inversion and error analysis, closely following the procedure of Korenaga et al. (2000). The large high-velocity lower crust seen in the model of White et al. (1987) is considerably smaller in the newer Hatton Bank model, and the thicker part of their transect exhibits a negative correlation between crustal V_p and thickness (Figure 12c), similar to the SIGMA-2 transect. Instead of calling for a chemically different source mantle, however, White et al. (2008) offered a new interpretation: the part of the crustal model that exhibits the negative correlation contains some preexisting continental crust. They then focused mainly on the remaining part of their transect, which exhibits a positive correlation between crustal V_p and thickness. Unfortunately, this thinner part of the transect is susceptible to the effects of porosity and alteration. As a result, the positive correlation does not necessarily require a change in mantle potential temperature during melt generation.

If we exclude the thicker part of the SIGMA-2 and Hatton Bank transects as being influenced by the preexisting continental crust, and if we exclude the thinner part of those transects as being unreliable owing to the effects of porosity and alteration, then there would be no part left for petrological interpretation. Nonetheless, the hypothesis that there is a significant amount of preexisting continental crust within the continent-ocean transition is difficult to reject. The only major concern would be that, if we apply the strategy of White et al. (2008) to the SIGMA-2 model (i.e., ascribing the part with "too low" crustal V_p to incorporation of extended continental crust), the preexisting continental crust has to be extended over ~200 km (Figure 12b), instead of only ~50 km in case of the Hatton Bank transect. Continental rifting can exhibit a variety of styles depending on crustal and mantle rheology (e.g., Buck, 1991; Geoffroy et al., 2015; Huismans & Beaumont, 2003, 2011; Petersen et al., 2018), so that 200 km of extension may not be unreasonable. Moreover, the interpretation shown in Figure 12b is consistent with the interpretation of the Hatton Bank transect by White et al. (2008) in one additional respect. On both transects, the presumed extended continental crust coincides with the surface distribution of seaward-dipping reflectors (SDRs). On the SIGMA-2 transect, SDRs are observed up to km 240 (Korenaga et al., 2000). The formation of SDRs indicates subaerial eruption (Hinz, 1981; Mutter et al., 1982) and does not require the presence of extended continental crust. However, reduced crustal density due to incorporation of buoyant, felsic continental crust could contribute to raising the locus of volcanism above sea level.

To summarize, there are three contentious points. The first is the meaning of high-velocity lower crust. If the average V_p of lower crust is only ~7.3 km s^{-1}, it does not necessarily require the melting of a hotter-than-normal mantle; it may be explained by the reduced effects of crack porosity and seawater alteration at high pressures. The second is the accuracy of crustal velocity models. Extensive regions of high-velocity lower crust, such as are illustrated in the classic papers of White et al. (1987) and White and McKenzie (1989), are not imaged in more contemporary analyses of better seismic data. The third is how to interpret the thicker part of transitional crust. For petrological interpretation, this part is more meaningful than the thinner part because the latter suffers from the possible effects of crack porosity and seawater alteration. But this thicker part is adjacent to the continental crust, so the influence of extended continental crust is hard to dismiss. With these caveats in mind, we now proceed to the interpretation of the SIGMA-1 velocity model.

5.2. Geological Interpretation of the SIGMA-1 Crustal Structure

To quantitatively compare the SIGMA-1 transect with other transects in the North Atlantic margins, average lower-crustal velocity and whole-crustal thickness are calculated from km 70 to km 250, at an interval of

20 km with a 20-km-wide averaging window, using all of 401 optimal models (Figure 13). We followed the temperature and pressure correction procedure of Korenaga et al. (2002), and for the temperature correction, we assumed a linear conductive geotherm with a thermal gradient of 16 K km^{-1} and a surface temperature of 0°C. As mentioned earlier, we need to focus on lower-crustal velocity because the upper-crustal velocity can be significantly lowered by porosity and alteration, which may not contain useful petrological information. We can use lower-crustal velocity as an upper bound on the possible range of bulk crustal velocity, given the cumulate nature of oceanic lower crust (Korenaga et al., 2002). We specify the lower-crustal section as the region below the 6.5 km s^{-1} V_p contour, at which velocity gradients change sharply (section 4.1). Relatively large model uncertainties (Figure 9d) are reflected in the greater uncertainty in the velocity-thickness covariation than along the SIGMA-2 and the Hatton Bank transects. In what follows, therefore, we limit ourselves on the most robust aspects of the velocity-thickness covariation.

Whereas the crustal thickness varies almost linearly along the SIGMA-1 transect (Figure 9c), the velocity-thickness covariation exhibits a clear west-east dichotomy (Figure 13). The western half of the transect (km <150) is characterized by an average lower-crustal V_p of ~6.8±0.1 km s^{-1}. Such lower-crustal compressional wave speed, together with the observed crustal thickness of 30–35 km, closely matches the average crustal structure of continental crust in an extensional tectonic setting (Christensen & Mooney, 1995). Thus, it is possible that the western half is made almost entirely of extended continental crust (Figure 13c). However, the 6.5 km s^{-1} V_p contour, which is used to divide upper and lower crust for the most of the transect, plunges down to >20 km depth near the western end, and this apparently very thick "upper crust" is a robust feature (region E in Figure 11). This is similar to what is seen in the SIGMA-2 transect, so as in its original interpretation (Figure 12a), we may also interpret that the continental crust is terminated at around km 60 (Figure 13d).

The eastern half of the transect (km >150) is characterized by slightly thinner crust (~27±2 km) and an average lower-crustal V_p of ~7.0±0.15 km s^{-1}. The part of the transect around km 170 stands out for its high lower-crustal V_p (>7.5 km s^{-1}; Figure 9c), which is one of the robust features of our model (region D in Figure 11) and likely represents mafic to ultramafic cumulates associated with the emplacement of plutonic rocks. However, the average lower-crustal V_p for this part is still only ~7.2 km s^{-1}, that is, lower than expected for the *P*-wave speed of pristine oceanic lower crust (~7.3 km s^{-1}). And the crust is thick enough that its compressional wave speed is probably not affected by porosity or alteration. However, the most striking aspect of the eastern half is that most of it is nearly indistinguishable from the thickest part of the SIGMA-2 crustal model (Figure 13). As a result, it shares the ambiguity associated with the petrological interpretation of the SIGMA-2 velocity model. That is, the eastern half of the SIGMA-1 crustal model may reflect incorporation of a substantial amount of extended continental crust (Figure 13a) or igneous crust formed as a result of moderately active upwelling of an anomalously fertile (Figure 13b).

In-depth comparison among SIGMA-1, SIGMA-2, and Hatton Bank transects (Figure 14) further supports that the SIGMA-1 transect is characterized by anomalously low V_p, particularly for the lower crust of the western part. In the SIGMA-2 transect, only the western end of the transect is similar to the continental part of Hatton Bank, but this similarity persists more toward the middle of the SIGMA-1 transect. On the SIGMA-1 transect, some part of the lower crust exhibits velocity inversion, with positive velocity anomalies just below the high-velocity-gradient upper crust (see km 60, km 120, and km 220), and this is a robust feature (Figure 11). These isolated velocity anomalies may correspond to mafic intrusion in the extended continental crust. In Figure 9c, the region at around km 170 appears to have strikingly high V_p lower crust, but the region is actually not very different from the continent-ocean transition at Hatton Bank (Figure 14b). The high V_p lower crust is simply accentuated by being in the middle of generally low V_p.

The SIGMA-1 transect is different from the SIGMA-2 or Hatton Bank transects, in that it is on the Greenland-Iceland Ridge and thus considered to be part of the Iceland hotspot track. Thus, whatever interpretation we adopt for the SIGMA-1 crustal model may also be valid for the Icelandic crust itself. Even if this is the case, both of the two different interpretations seem to be possible. Major element heterogeneity in the source mantle has been suggested for both East Greenland and Southwest Iceland (Korenaga & Kelemen, 2000), so the spatial extent of anomalously fertile mantle may be sufficiently large. At the same time, the entire Greenland-Iceland Ridge is covered by SDRs (Figure 15), so the possible correlation between the presumed, extended continental crust and SDRs could still be consistent with observations.

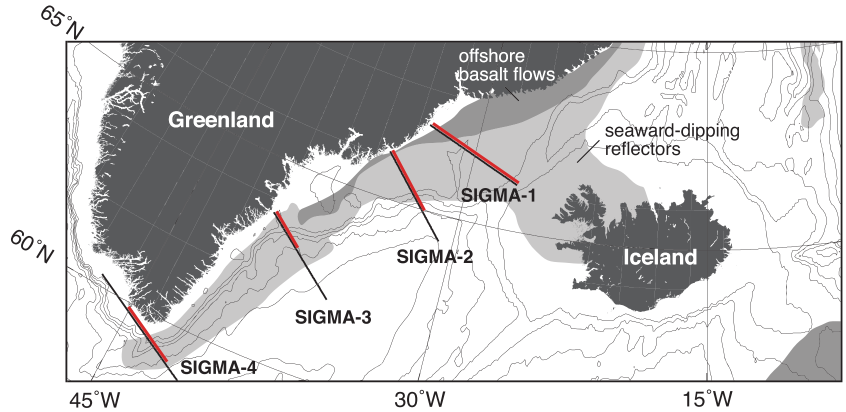

Figure 15. Distribution of seaward-dipping reflectors (light gray) and offshore basalt flows (dark gray) along the East Greenland margin (Larsen et al., 2014) and the location of SIGMA transects. Red lines indicate the location of thick (>15 km) crust with relatively low V_p, based on the velocity models of this study (SIGMA-1), Korenaga et al. (2000) (SIGMA-2), Hopper et al. (2003) (SIGMA-3), and Holbrook et al. (2001) (SIGMA-4).

To reiterate, if the thick crust of the Greenland-Iceland Ridge and its shallow bathymetry owe much to incorporation of extended continental crust, then the continuity between the Greenland-Iceland Ridge and Iceland suggests that the thick Icelandic crust might also contain a significant amount of continental crust. Given the status of the Iceland hotspot in the literature, as the archetypical example of plume-ridge interaction (e.g., Ito et al., 1999; Sleep, 1990), this suggestion may appear to be too radical. However, the possibility that the part of the Icelandic crust may be continental has occasionally been raised in the past (Foulger, 2006; Torsvik et al., 2015). Recently, a more comprehensive hypothesis that Iceland, along with the Greenland-Iceland-Faroe Ridge, is largely continental, has been put forward by Foulger et al. (2020), based on a diverse array of observations and theoretical inferences, including the seismic velocity of the Icelandic lower crust, the petrology and geochemistry of the Icelandic lavas, and the tectonic history of the opening of the North Atlantic.

There are well-documented examples of incorporation of continental material in the center of ocean basins and in oceanic plateaus. There are Paleozoic sediments (presumably underlain by some extended continental crust) near the equatorial Mid-Atlantic Ridge (Bonatti et al., 1996), perhaps due to repeated ridge jumps during opening of the Atlantic at this latitude. Similarly, the Kerguelen Plateau, commonly interpreted as a plume-related large igneous province, demonstrably contains continental material recovered during ocean drilling (e.g., Frey et al., 2002; Ingle et al., 2002). However, Foulger et al. (2020) invoke much more extensive incorporation of continental crust than previous workers. It remains to be seen whether their proposed mechanism, with continental crust flowing from distal regions into the IGR and IFR for tens of millions of years, is physically feasible. Moreover, it should be noted that no inherited zircons, and no xenoliths of continental material, have been observed in Iceland, though both young zircons and mafic xenoliths are found in the extensive outcrops there.

On the other hand, thick crust with relatively low V_p along the Greenland-Iceland Ridge could be due to melting of regionally extensive source mantle heterogeneities combined with active mantle upwelling (e.g., Korenaga, 2004; Korenaga & Kelemen, 2000; Korenaga et al., 2002; Shorttle & Maclennan, 2011). This hypothesis remains consistent with all available data. The narrow, laterally extensive nature of the GIR and IFR is consistent with active mantle upwelling in and around the Iceland plume during opening of the Atlantic. Although the Iceland hotspot and its peripheral areas such as the GIR and the Reykjanes Ridge are usually explained as the consequences of a purely thermal plume, it is important to recognize that it is not a unique interpretation. For example, V-shaped ridges along the Reykjanes Ridge have long been explained by thermal fluctuations in the plume (the "pulsing plume" hypothesis of Vogt (1971)) (e.g., Ito, 2001; White, 1997), but recent marine geophysical surveys have shown that, contrary to the prediction of the pulsing plume hypothesis, the V-shaped ridges are not symmetric about the Reykjanes Ridge (Hey et al., 2010) and that the tectonic evolution of the ridge involves multiple rift propagation events, which is difficult to explain by a simple thermal model (Hey et al., 2016).

6. Summary and Outlook

We analyzed the ocean-bottom seismic data collected along the Greenland-Iceland Ridge and constructed a new crustal velocity model. Whereas the seismic data were of moderate quality, we strove to make the most of them by applying the travel-time tomography of Korenaga and Sager (2012), an upgrade of the original approach of Korenaga et al. (2000) with adaptive importance sampling. Crustal thickness along the SIGMA-1 transect is ∼30 km on average, though it varies gradually, with the western half being ∼5 km thicker than the eastern half. Furthermore, the western and eastern parts are distinct from each other in average lower-crustal V_p. On the basis of crustal thickness and compressional wave speed, as well as its proximity to Greenland, the western part could be predominantly composed of extended continental crust. The average lower-crustal V_p of the eastern part is higher than that of the western part, but it is still too low to be interpreted as the result of the melting of a hot mantle plume with a "normal" mantle composition. The eastern part of the SIGMA-1 crustal model closely resembles the thickest part of the SIGMA-2 crustal model, so considering the existing interpretations for the SIGMA-2 model, we suggest that the formation of the Greenland-Iceland Ridge requires an anomalously fertile source mantle or substantial incorporation of extended continental crust. The latter possibility supports the recent hypothesis that Iceland and the Greenland-Iceland-Faroe Ridge contain a substantial amount of continental crust. Thus, contrary to our initial expectation, the ambiguity in interpreting seismic data for continent-ocean transition is not diminished in the SIGMA-1 transect.

Whereas the Icelandic crust has been studied by a number of passive- and active-source experiments (e.g., Bjarnason et al., 1993; Darbyshire et al., 2000; Foulger et al., 2003; Menke et al., 1998), the crustal structure of the Greenland-Iceland-Faroe Ridge is much less constrained. As the existing seismic data collected from the Iceland-Faroe Ridge are of poor quality (Richardson et al., 1998), the SIGMA-1 data from the Greenland-Iceland Ridge are of critical importance to test the continental hypothesis of Foulger et al. (2020). If the Icelandic lower crust is mostly continental, as suggested by Foulger et al. (2020), then only 1/3 to 1/4 of the total Icelandic crust would have resulted from mantle melting, thereby lowering the inferred contribution from melting of the Iceland plume. The plume buoyancy flux for Iceland has been estimated to be ∼1.4 Mg s^{-1} (King & Adam, 2014; Sleep, 1990), but given the above consideration, it could be reduced to ∼0.4 Mg s^{-1}, which is only ∼1/20 of the buoyancy flux of the Hawaiian plume.

Data Availability Statement

The SIGMA-1 data are available from the Marine-Geo Digital Library of the Marine Geoscience Data System (http://www.marine-geo.org/tools/entry/EW9607). The DOIs for OBS and OBH data sets are, respectively, doi:10.26022/IEDA/327349 and doi:10.26022/IEDA/327350.

Acknowledgments
The authors thank constructive suggestions from Eduardo Contreras-Reyes, Bob White, and an anonymous reviewer.

References

Allen, R. M., Nolet, G., Morgan, W. J., Vogfjörd, K., Bergsson, B. H., Erlendsson, P., et al. (2002). Imaging the mantle beneath Iceland using integrated seismological techniques. *Journal of Geophysical Research*, *107*, 2325. https://doi.org/10.1029/2001JB000595

Aster, R. C., Borchers, B., & Thurber, C. H. (2005). *Parameter estimation and inverse problems*. Cambridge, MA: Academic Press.

Barton, A. J., & White, R. S. (1997). Crustal structure of Edoras Bank continental margin and mantle thermal anomalies beneath the North Atlantic. *Journal of Geophysical Research*, *102*(B2), 3109–3129. https://doi.org/10.1029/96JB03387

Behn, M. D., & Kelemen, P. B. (2003). Relationship between seismic P-wave velocity and the composition of anhydrous igneous and meta-igneous rocks. *Geochemistry, Geophysics, Geosystems*, *4*(5), 1041. https://doi.org/10.1029/2002GC00393

Bijwaard, H., & Spakman, W. (1999). Tomographic evidence for a narrow whole mantle plume below Iceland. *Earth and Planetary Science Letters*, *166*, 121–126.

Bjarnason, I. T., Menke, W., Flovenz, G., & Caress, D. (1993). Tomographic image of the Mid-Atlantic plate boundary in southwestern Iceland. *Journal of Geophysical Research*, *98*(B4), 6607–6622. https://doi.org/10.1029/92JB02412

Bonatti, E., Ligi, M., Borsetti, A. M., Gasperini, L., Negri, A., & Sartori, R. (1996). Lower Cretaceous deposits trapped near the equatorial Mid-Atlantic Ridge. *Nature*, *380*, 518–520.

Bott, M. H. P. (1983). Deep structure and geodynamics of the Greenland-Scotland Ridge: An introductory review, *Structure and development of the Greenland-Scotland Ridge* (pp. 3–9): Springer.

Brown, E. L., & Lesher, C. E. (2014). North Atlantic magmatism controlled by temperature, mantle composition and buoyancy. *Nature Geoscience*, *7*, 820–824.

Buck, W. R. (1991). Modes of continental lithospheric extension. *Journal of Geophysical Research*, *96*(B12), 20,161–20,178. https://doi.org/10.1029/91JB01485

Chesley, C., Key, K., Constable, S., Behrens, J., & MacGregor, L. (2019). Crustal cracks and frozen flow in oceanic lithosphere inferred from electrical anisotropy. *Geochemistry, Geophysics, Geosystems*, *20*, 5979–5999. https://doi.org/10.1029/2019GC008628

Christensen, N. I., & Mooney, W. D. (1995). Seismic velocity structure and composition of the continental crust: A global view. *Journal of Geophysical Research*, *100*(B6), 9761–9788. https://doi.org/10.1029/95JB00259

Christensen, N. I., & Smewing, J. D. (1981). Geology and seismic structure of the northern section of the Oman ophiolite. *Journal of Geophysical Research*, *86*(B4), 2545–2555. https://doi.org/10.1029/JB086iB04p02545

Coffin, M. F., & Eldholm, O. (1994). Large igneous provinces: Crustal structure, dimensions, and external consequences. *Reviews of Geophysics*, *32*, 1–36.

Darbyshire, F. A., Priestley, K. F., White, R. S., Stefansson, R., Gudmundsson, G. B., & Jakobsdottir, S. (2000). Crustal structure of central and northern Iceland from analysis of teleseismic receiver functions. *Geophysical Journal International*, *143*, 163–184.

Du, Z., Vinnik, L. P., & Foulger, G. R. (2006). Evidence from P-to-S mantle converted waves for a flat “660-km” discontinuity beneath Iceland. *Earth and Planetary Science Letters*, *241*, 271–280.

Eccles, J. D., White, R. S., & Christie, P. A. F. (2011). The composition and structure of volcanic rifted continental margins in the North Atlantic: Further insight from shear waves. *Tectonophysics*, *508*, 22–33.

Foulger, G. R. (2006). Older crust underlies Iceland. *Geophysical Journal International*, *165*, 672–676.

Foulger, G. R., & Anderson, D. L. (2005). A cool model for the Iceland hotspot. *Journal of Volcanology and Geothermal Research*, *141*, 1–22.

Foulger, G. R., Dore, T., Emeleus, C. H., Franke, D., Geoffroy, L., Gernigon, L., & Stoker, M. (2020). The Iceland Microcontinent and a continental Greenland-Iceland-Faroe-Ridge. *Earth-Science Reviews*. https://doi.org/10.1016/j.earscirev.2019.102926

Foulger, G. R., Du, Z., & Julian, B. R. (2003). Icelandic-type crust. *Geophysical Journal International*, *155*, 567–590.

Foulger, G. R., Pritchard, M. J., Julian, B. R., Evans, J. R., Allen, R. M., Nolet, G., et al. (2000). The seismic anomaly beneath Iceland extends down to the mantle transition zone and no deeper. *Geophysical Journal International*, *142*, F1–F5.

Fowler, S. R., White, R. S., Spence, G. D., & Westbrook, G. K. (1989). The Hatton Bank continental margin—II. Deep structure from two-ship expanding spread seismic profiles. *Geophysical Journal International*, *96*, 295–309.

French, S. W., & Romanowicz, B. (2015). Broad plumes rooted at the base of the Earth's mantle beneath major hotspots. *Nature*, *525*, 95–99.

Frey, F. A., Weis, D., Borisova, A. Y., & Xu, G. (2002). Involvement of continental crust in the formation of the Cretaceous Kerguelen Plateau: New perspectives from ODP Leg 120 Sites. *Journal of Petrology*, *43*, 1207–1239.

Geoffroy, L., Burov, E. B., & Werner, P. (2015). Volcanic passive margins: Another way to break up continents. *Scientific Reports*, *5*, 14,828. https://doi.org/10.1038/srep14828

Griffiths, R. W., & Campbell, I. H. (1990). Stirring and structure in mantle starting plumes. *Earth and Planetary Science Letters*, *99*, 66–78.

He, Y., Wen, L., Capdeville, Y., & Zhao, L. (2015). Seismic evidence for an Iceland thermo-chemical plume in the Earth's lowermost mantle. *Earth and Planetary Science Letters*, *417*, 19–27.

Helmberger, D. V., Wen, L., & Ding, X. (1998). Seismic evidence that the source of the Iceland hotspot lies at the core-mantle boundary. *Nature*, *396*, 251–255.

Herzberg, C., Asimow, P. D., Arndt, N., Niu, Y., Lesher, C. M., Fitton, J. G., et al. (2007). Temperatures in ambient mantle and plumes: Constraints from basalts, picrites, and komatiites. *Geochemistry, Geophysics, Geosystems*, *8*, Q02206. https://doi.org/10.1029/2006GC001390

Hey, R., Martinez, F., Hoskuldsson, A., & Benediktsdottir, A. (2010). Propagating rift model for the V-shaped ridges south of Iceland. *Geochemistry, Geophysics, Geosystems*, *11*, Q03011. https://doi.org/10.1029/2009GC002865

Hey, R., Martinez, F., Hoskuldsson, A., Eason, D. E., Sleeper, J., Thordarson, S., et al. (2016). Multibeam investigation of the active North Atlantic plate boundary reorganization tip. *Earth and Planetary Science Letters*, *435*, 115–123.

Hinz, K. (1981). A hypothesis on terrestrial catastrophes wedges of very thick oceanward dipping layers beneath passive continental margins. *Geologisches Jahrbuch / E*, *22*, 3–28.

Holbrook, W. S., Larsen, H. C., Korenaga, J., Dahl-Jensen, T., Reid, I. D., Kelemen, P. B., et al. (2001). Mantle thermal structure and melting processes during continental breakup in the North Atlantic. *Earth and Planetary Science Letters*, *190*, 251–266.

Holbrook, W. S., Purdy, G. M., Sheridan, R. E., Glover III, L., Talwani, M., Ewing, J., et al. (1994). Seismic structure of the U.S. Mid-Atlantic continental margin. *Journal of Geophysical Research*, *99*(B9), 17,871–17,891. https://doi.org/10.1029/94JB00729

Hopper, J. R., Dalh-Jensen, T., Holbrook, W. S., Larsen, H. C., Lizarralde, D., Korenaga, J., et al. (2003). Structure of the SE Greenland margin from seismic reflection and refraction data: Implications for nascent spreading center subsidence and asymmetric crustal accretion during North Atlantic opening. *Journal of Geophysical Research*, *108*(B5), 2269. https://doi.org/10.1029/2002JB001996

Huismans, R., & Beaumont, C. (2003). Symmetric and asymmetric lithospheric extension: Relative effects of frictional-plastic and viscous strain softening. *Journal of Geophysical Research*, *108*, 2496. https://doi.org/10.1029/2002JB002026

Huismans, R., & Beaumont, C. (2011). Depth-dependent extension, two-stage breakup and cratonic underplating at rifted margins. *Nature*, *473*, 74–78.

Ingle, S., Weis, D., & Frey, F. A. (2002). Indian continental crust recovered from Elan Bank, Kerguelen Plateau (ODP Leg 183, Site 1137). *Journal of Petrology*, *43*, 1241–1257.

Ito, G. (2001). Reykjanes ‘V’-shaped ridges originating from a pulsing and dehydrating mantle plume. *Nature*, *411*, 681–684.

Ito, G., Shen, Y., Hirth, G., & Wolfe, G. J. (1999). Mantle flow, melting, and dehydration of the Iceland mantle plume. *Earth and Planetary Science Letters*, *165*, 81–96.

Jenkins, J., Cottaar, S., White, R. S., & Deuss, A. (2016). Depressed mantle discontinuities beneath Iceland: Evidence of a garnet controlled 660 km discontinuity? *Earth and Planetary Science Letters*, *433*, 159–168.

Keen, C. E., & Boutilier, R. R. (1995). Lithosphere-asthenosphere interactions below rifts. In *Rifted Ocean-Continent Boundaries*, Kluwer, pp. 17–30.

Kelemen, P. B., & Holbrook, W. S. (1995). Origin of thick, high-velocity igneous crust along the U.S. East Coast Margin. *Journal of Geophysical Research*, *100*(B6), 10,077–10,094. https://doi.org/10.1029/95JB00924

King, S. D., & Adam, C. (2014). Hotspot swells revisited. *Physics of the Earth and Planetary Interiors*, *235*, 66–83.

Korenaga, J. (2004). Mantle mixing and continental breakup magmatism. *Earth and Planetary Science Letters*, *218*, 463–473.

Korenaga, J. (2007). Thermal cracking and the deep hydration of oceanic lithosphere: A key to the generation of plate tectonics? *Journal of Geophysical Research*, *112*, B05408. https://doi.org/10.1029/2006JB004502

Korenaga, J. (2011). Velocity-depth ambiguity and the seismic structure of large igneous provinces: A case study from the Ontong Java Plateau. *Geophysical Journal International*, *185*, 1022–1036.

Korenaga, J. (2017). On the extent of mantle hydration by plate bending. *Earth and Planetary Science Letters*, *457*, 1–9.

Korenaga, J., Holbrook, W. S., Kent, G. M., Kelemen, P. B., Detrick, R. S., Larsen, H. C., et al. (2000). Crustal structure of the southeast Greenland margin from joint refraction and reflection seismic tomography. *Journal of Geophysical Research*, *105*(B9), 21,591–21,614. https://doi.org/10.1029/2000JB900188

Korenaga, J., & Jordan, T. H. (2001). Effects of vertical boundaries on infinite Prandtl number thermal convection. *Geophysical Journal International*, *147*, 639–659.

Korenaga, J., & Jordan, T. H. (2002). On the state of sublithospheric upper mantle beneath a supercontient. *Geophysical Journal International*, *149*, 179–189.

Korenaga, J., & Kelemen, P. B. (2000). Major element heterogeneity of the mantle source in the North Atlantic igneous province. *Earth and Planetary Science Letters*, *184*, 251–268.

Korenaga, J., Kelemen, P. B., & Holbrook, W. S. (2002). Methods for resolving the origin of large igneous provinces from crustal seismology. *Journal of Geophysical Research*, *107*(B9), 2178. https://doi.org/10.1029/2001JB001030

Korenaga, T., & Korenaga, J. (2016). Evolution of young oceanic lithosphere and the meaning of seafloor subsidence rate. *Journal of Geophysical Research: Solid Earth*, *121*, 6315–6332. https://doi.org/10.1002/2016JB013395

Korenaga, J., & Sager, W. W. (2012). Seismic tomography of Shatsky Rise by adaptive importance sampling. *Journal of Geophysical Research*, *117*, B08102. https://doi.org/10.1029/2012JB009248

Larsen, H. C., & Jakobsdóttir, S. (1988). Distribution, crustal properties and significance of seawards-dipping sub-basement reflectors off E Greenland. In A. C. Morton, & L. M. Parson (Eds.), *Early Tertiary Volcanism and the Opening of the NE Atlantic* (Vol. 39, pp. 95–114).

Larsen, L. M., Pedersen, A. K., Tegner, C., & Duncan, R. A. (2014). Eocene to Miocene igneous activity in NE Greenland: Northward younging of magmatism along the East Greenland margin. *Journal of the Geological Society*, *171*, 539–553.

Lawver, L. A., & Müller, R. D. (1994). Iceland hotspot track. *Geology*, *22*, 311–314.

Lévěque, J. J., Rivera, L., & Wittlinger, G. (1993). On the use of the checker-board test to assess the resolution of tomographic inversions. *Geophysical Journal International*, *115*, 313–318.

McKenzie, D., & Bickle, M. J. (1988). The volume and composition of melt generated by extension of the lithosphere. *Journal of Petrology*, *29*, 625–679.

Menke, W., West, M., Brandsdottir, B., & Sparks, D. (1998). Compressional and shear velocity structure of the lithosphere in northern Iceland. *Bulletin of the Seismological Society of America*, *88*, 1561–1571.

Mihalffy, P., Steinberger, B., & Schmeling, H. (2008). The effect of the large-scale mantle flow field on the Iceland hotspot track. *Tectonophysics*, *447*, 5–18.

Mjelde, R., Digranes, P., Shimamura, H., Shiobara, H., Kodaira, S., Brekke, H., et al. (1998). Crustal structure of the northern part of the Vøring Basin, mid-Norway margin, from wide-angle seismic and gravity data. *Tectonophysics*, *293*, 175–205.

Montelli, R., Nolet, G., Dahlen, F. A., & Masters, G. (2006). A catalog of deep mantle plumes: New results from finite-frequency tomography. *Geochemistry, Geophysics, Geosystems*, *7*, Q11007. https://doi.org/10.1029/2006GC001248

Montelli, R., Nolet, G., Dahlen, F. A., Masters, G., England, E. R., & Hung, S. H. (2004). Finite-frequency tomography reveals a variety of plumes in the mantle. *Science*, *303*, 338–343.

Morgan, W. J. (1971). Convection plumes in the lower mantle. *Nature*, *230*, 42–43.

Morgan, J. V., Barton, P. J., & White, R. S. (1989). The Hatton Bank continental margin—III. Structure from wide-angle OBS and multichannel seismic refraction profiles. *Geophysical Journal International*, *96*, 367–384.

Moser, T. J. (1991). Shortest path calculation of seismic rays. *Geophysics*, *56*, 59–67.

Moser, T. J., Nolet, G., & Snieder, R. (1992). Ray bending revisited. *Bulletin of the Seismological Society of America*, *82*, 259–288.

Mutter, J. C., Talwani, M., & Stoffa, P. L. (1982). Origin of seaward-dipping reflectors in oceanic crust off the Norwegian margin by “subaerial sea-floor spreading”. *Geology*, *10*, 353–357.

Mutter, J. C., & Zehnder, C. M. (1988). Deep crustal structure and magmatic processes: The inception of seafloor spreading in the Norwegian-Greenland Sea. In A. C. Morton, & L. M. Parson (Eds.), *Early tertiary volcanism and the opening of the NE Atlantic* (Vol. 39, pp. 35–48). Malden, Mass: Blackwell Sci.

Nichols, A. R. L., Carroll, M. R., & Höskuldsson, A. (2002). Is the Iceland hot spot also wet? Evidence from the water contents of undegassed submarine and subglacial pillow basalts. *Earth and Planetary Science Letters*, *202*, 77–87.

Parkin, C. J., & White, R. S. (2008). Influence of the Iceland mantle plume on oceanic crust generation in the North Atlantic. *Geophysical Journal International*, *173*, 168–188.

Petersen, K. D., Schiffer, C., & Nagel, T. (2018). LIP formation and protracted lower mantle upwelling induced by rifting and delamination. *Scientific Reports*, *8*, 16,578. https://doi.org/10.1038/s41598-018-34194-0

Rawlinson, N., Fichtner, A., Sambridge, M., & Young, M. K. (2014). Seismic tomography and the assessment of uncertainty. *Advances in Geophysics*, *55*, 1–76.

Richards, M., Contreras-Reyes, E., Lithgow-Bertelloni, C., & Ghiorso, M. (2013). Petrological interpretation of deep crustal intrusive bodies beneath oceanic hotspot provinces. *Geochemistry, Geophysics, Geosystems*, *14*, 604–619. https://doi.org/10.1029/2012GC004448

Richards, M. A., Duncan, R. A., & Courtillot, V. E. (1989). Flood basalts and hot-spot tracks: Plume heads and tails. *Science*, *246*, 103–107.

Richardson, K. R., Smallwood, J. R., White, R. S., Snyder, D. B., & Maguire, P. K. H. (1998). Crustal structure beneath the Faroe Islands and the Faroe-Iceland Ridge. *Tectonophysics*, *300*, 159–180.

Rickers, F., Fichtner, A., & Trampert, J. (2013). The Iceland-Jan Mayen plume system and its impact on mantle dynamics in the North Atlantic region: Evidence from full-waveform inversion. *Earth and Planetary Science Letters*, *367*, 39–51.

Ritsema, J., Deuss, A., van Heijst, H. J., & Woodhouse, J. H. (2011). S40RTS: A degree-40 shear-velocity model for the mantle from new Rayleigh wave dispersion, teleseismic traveltime and normal-mode splitting function measurements. *Geophysical Journal International*, *184*, 1223–1236.

Sallares, V., Charvis, P., Flueh, E. R., Bialas, J., & Party, T. S. S. (2005). Seismic structure of the Carnegie ridge and the nature of the Galapagos hotspot. *Geophysical Journal International*, *161*, 763–788.

Shen, Y., Solomon, S. C., Bjarnason, I. T., Nolet, G., Morgan, W. J., Allen, R. M., et al. (2002). Seismic evidence for a tilted mantle plume and north–south mantle flow beneath Iceland. *Earth and Planetary Science Letters*, *197*, 261–272.

Shen, Y., Solomon, S. C., Bjarnason, I. T., & Wolfe, C. J. (1998). Seismic evidence for a lower mantle origin of the Iceland plume. *Nature*, *395*, 62–65.

Shorttle, O., & Maclennan, J. (2011). Compositional trends of Icelandic basalts: Implications for short-length scale lithological heterogeneity in mantle plumes. *Geochemistry, Geophysics, Geosystems*, *12*, Q11008. https://doi.org/10.1029/2011GC003748

Skogseid, J., Planke, S., Faleide, J. I., Pedersen, T., Eldholm, O., & Neverdal, F. (2000). NE Atlantic continental rifting and volcanic margin formation. In A. Nøttvedt (Ed.), *Dynamics of the Norwegian Margin* (pp. 295–326): Geological Society of London.

Sleep, N. H. (1990). Hotspots and mantle plumes: Some phenomenology. *Journal of Geophysical Research*, *95*(B5), 6715–6736. https://doi.org/10.1029/JB095iB05p06715

Smallwood, J. R., Staples, R. K., Richardson, K. R., & White, R. S. (1999). Crust generated above the Iceland mantle plume: From continental rift to oceanic spreading center. *Journal of Geophysical Research*, *104*(B10), 22,885–22,902. https://doi.org/10.1029/1999JB900176

Smallwood, J. R., & White, R. S. (2002). Ridge-plume interaction in the North Atlantic and its influence on continental breakup and seafloor spreading. In D. W. Jolley, & B. R. Bell (Eds.), *The North Atlantic Igneous Province: Stratigraphy, tectonic, volcanic and magmatic processes* pp. 15–37): Geological Society of London.

Straume, E. O., Gaina, C., Medvedev, S., Hochmuth, K., Gohl, K., Whittaker, J. M., et al. (2019). GlobSed: Updated total sediment thickness in the world's oceans. *Geochemistry, Geophysics, Geosystems*, *20*, 1756–1772. https://doi.org/10.1029/2018GC008115

Toomey, D. R., & Foulger, G. R. (1989). Tomographic inversion of local earthquake data from the Hengill-Grensdalur central volcano complex, Iceland. *Journal of Geophysical Research*, *94*(B12), 17,497–17,510. https://doi.org/10.1029/JB094iB12p17497

Torsvik, T. H., Amundsen, H. E. F., Trønnes, R. G., Doubrovine, P. V., Gaina, C., Kusznir, N. J., et al. (2015). Continental crust beneath southeast Iceland. *Proceedings of the National Academy of Sciences of the United States of America*, *112*, E1818–E1827.

Vinnik, L. P., Foulger, G. R., & Du, Z. (2005). Seismic boundaries in the mantle beneath Iceland: A new constraint on temperature. *Geophysical Journal International*, *160*, 533–538.

Vogt, P. R. (1971). Asthenosphere motion recorded by the ocean floor south of Iceland. *Earth and Planetary Science Letters*, *13*, 153–160.

Vogt, P. R. (1991). Bermuda and Appalachian-Labrador rises: Common non-hotspot processes? *Geology*, *19*, 41–44.

White, R. S. (1997). Rift-plume interaction in the North Atlantic. *Philosophical transactions of the Royal Society of London*, *355*, 319–339.

White, R., & McKenzie, D. (1989). Magmatism at rift zones: The generation of volcanic continental margins and flood basalts. *Journal of Geophysical Research*, *94*(B6), 7685–7729. https://doi.org/10.1029/JB094iB06p07685

White, R. S., McKenzie, D., & O'Nions, R. K. (1992). Oceanic crustal thickness from seismic measurements and rare earth element inversions. *Journal of Geophysical Research*, *97*(B13), 19,683–19,715. https://doi.org/10.1029/92JB01749

White, R. S., & Smith, L. K. (2009). Crustal structure of the Hatton and the conjugate east Greenland rifted volcanic continental margins, NE Atlantic. *Journal of Geophysical Research*, *114*, B02305. https://doi.org/10.1029/2008JB005856

White, R. S., Smith, L. K., Roberts, A. W., Christie, P. A. F., Kusznir, N. J., & iSIMM Team (2008). Lower-crustal intrusion on the North Atlantic continental margin. *Nature*, *452*, 460–464.

White, R. S., Spence, G. D., Fowler, S. R., McKenzie, D. P., Westbrook, G. K., & Bowen, A. N. (1987). Magmatism at rifted continental margins. *Nature*, *330*, 439–444.

Wolfe, C. J., Bjarnason, I. T., VanDecar, J. C., & Solomon, S. C. (1997). Seismic structure of the Iceland mantle plume. *Nature*, *385*, 245–247.

Yuan, K., & Romanowicz, B. (2017). Seismic evidence for partial melting at the root of major hot spot plumes. *Science*, *357*, 393–397.

Zehnder, C. M., Mutter, J. C., & Buhl, P. (1990). Deep seismic and geochemical constraints on the nature of rift-induced magmatism during breakup of the North Atlantic. *Tectonophysics*, *173*, 545–565.

Zhang, J. (1997). Nonlinear refraction and reflection traveltime tomography (Ph.D.), Mass. Inst. of Technol.

Zhang, J., Brink, U. S., & Toksöz, M. N. (1998). Nonlinear refraction and reflection travel time tomography. *Journal of Geophysical Research*, *103*, 29,743–29,757. https://doi.org/10.1029/98JB01981

Zhang, J., & Toksöz, M. N. (1998). Nonlinear refraction traveltime tomography. *Geophysics*, *63*, 1726–1737.